Global Biogeochemical Cycles

RESEARCH ARTICLE
10.1029/2024GB008249

Pacific-Arctic Ocean Acidification: Decadal Trends and Drivers

Thomas Caero[1], Hongjie Wang[1], and Annika Jersild[2]

[1]University of Rhode Island, Graduate School of Oceanography (URI-GSO), Narragansett, RI, USA, [2]University of Maryland - College Park, Earth System Science Interdisciplinary Center (ESSIC), College Park, MD, USA

Key Points:

- From 1993 to 2021, the Southern Pacific-Arctic Region (PAR) acidified at a similar rate to the global mean, primarily due to anthropogenic carbon dioxide uptake
- Bering Strait surface waters exhibited slower acidification trends during the same time period, likely due to increased primary productivity
- Anthropogenic CO_2, freshwater addition, and sea ice dynamics during this time caused the Northern PAR, and Beaufort Gyre in particular, to acidify 2–4 times faster than the global mean rate

Supporting Information:

Supporting Information may be found in the online version of this article.

Correspondence to:

T. Caero,
thomas@caero.info

Citation:

Caero, T., Wang, H., & Jersild, A. (2025). Pacific-Arctic Ocean acidification: Decadal trends and drivers. *Global Biogeochemical Cycles*, *39*, e2024GB008249. https://doi.org/10.1029/2024GB008249

Received 29 MAY 2024
Accepted 14 FEB 2025

Abstract This study presents the first regional-scale analysis to quantify decadal trends and drivers of surface ocean acidification (OA) across the highly sensitive Pacific-Arctic Region (PAR) using a consistent trend methodology. From 1993 to 2021, the Southern PAR acidified at rates comparable to the global average, with pH_T declining by 0.018 units dec^{-1} and aragonite saturation state (Ω_{Ar}) decreasing by 0.063 units dec^{-1}, primarily driven by anthropogenic CO_2 uptake. In contrast, the Bering Strait exhibited slower acidification, with pH_T declining by 0.011 units dec^{-1} and Ω_{Ar} decreasing by 0.020 units dec^{-1}—substantially lower than previously reported—likely due to increased primary productivity. The Northern PAR experienced the most rapid acidification: pH_T decreased by 0.028 units dec^{-1} and Ω_{Ar} by 0.078 units dec^{-1}, with the Beaufort Gyre acidifying 2–4 times faster than the global mean. This rapid change was driven by rising atmospheric CO_2 and significant freshening linked to sea ice melt and increased riverine input, which reduced the ocean's buffering capacity. Continued warming will likely exacerbate acidification in regions transitioning from multi-year to seasonal ice. While local processes such as primary productivity can temporarily counteract OA, whether they can offset rising anthropogenic CO_2 levels remains unclear. This underscores the importance of biogeochemical models that integrate climatic and biological feedbacks, enabling accurate forecasts of OA changes and their impacts on marine ecosystems. These findings highlight the urgent need for sustained monitoring in the PAR, where accelerating changes threaten critical ecosystems.

Plain Language Summary Many human activities release carbon dioxide into the atmosphere, a significant portion of which is absorbed by the ocean. This process causes the ocean to become more acidic and can harm marine life. The Pacific-Arctic Region (PAR) is particularly vulnerable to acidification due to its unique chemical properties. The remote nature of this region makes data collection challenging and limits our understanding of long-term acidification trends. In our study, we used existing data sets and statistical methods to address these data gaps and determined surface acidification rates from 1993 to 2021 across the PAR. Our analysis revealed that surface waters in the Bering Strait acidified slowly, likely due to increased photosynthesis by plankton. Additionally, the Northern PAR acidified 2–4 times faster than the global average due to rising atmospheric CO_2 and freshwater addition. The freshwater primarily came from melting sea ice, which reduces the ocean's ability to resist acidification. This suggests that similar rapid acidification may soon occur in other locations where sea ice is melting. Our results emphasize the need for continuous research into this highly climate-sensitive region.

1. Introduction

The industrial revolution spawned an era where global atmospheric carbon dioxide (CO_2) levels have increased at a rate unparalleled in the last 65 million years (Honisch et al., 2012; Zeebe et al., 2016). This surge in CO_2 has been a major driver of global climate change (H. Lee et al., 2023; Pörtner et al., 2019) and has significantly altered ocean carbonate chemistry by increasing proton concentration ($[H^+]$) and decreasing carbonate concentration ($[CO_3^{2-}]$), reducing pH and calcium carbonate saturation states (Ω) (*i.e.*, ocean acidification) (Caldeira & Wickett, 2003; Doney et al., 2009; H. Lee et al., 2023; Orr et al., 2005; Pörtner et al., 2019). When CO_2 dissolves in seawater, it reacts with H_2O to form carbonic acid (H_2CO_3), which can dissociate into bicarbonate (HCO_3^-) and carbonate (CO_3^{2-}), releasing protons which lower pH. This shift in pH affects the relative proportion of the carbonate species—as water acidifies, free protons react with CO_3^{2-} to form HCO_3^-, decreasing $[CO_3^{2-}]$. The ocean carbonate system consists of H^+, OH^-, weak acid-base systems, and the four carbonate system parameters

and is resolvable to a known degree of uncertainty if temperature, salinity, pressure, and two of the four carbonate parameters are known (Dickson, 2007). The four carbonate system parameters are:

1. Dissolved inorganic carbon (DIC): the total concentration of carbonate species (carbonic acid, bicarbonate, carbonate).
2. Total alkalinity (TA): the ability for seawater to resist changes in acidity due to the concentration of excess proton acceptors relative to proton donors.
3. pH_T: pH on the total scale, which accounts for contributions from both free protons and hydrogen sulfate ions. It is defined as $pH_T = -\log_{10}([H^+]_F + [HSO_4^-])$, and serves as the standard for high-quality seawater pH measurements.
4. pCO_2: the partial pressure of CO_2 in seawater.

A consequence of decreased $[CO_3^{2-}]$ is the reduction in aragonite saturation state (Ω_{Ar}), which measures the thermodynamic tendency of aragonite (a form of calcium carbonate prevalent in seawater and marine organisms) to dissolve. Net dissolution of aragonite is thermodynamically favored when $\Omega_{Ar} < 1$. This adversely affects marine calcifiers by influencing their physiological functions (Doney et al., 2009; Feely et al., 2004; Orr et al., 2005), making it difficult to form and maintain their aragonite exoskeletons, and potentially disrupting overall ecosystem dynamics (AMAP, 2013, 2018; Cooley et al., 2009; H. Lee et al., 2023; Pörtner et al., 2019).

The global ocean has absorbed nearly a third of anthropogenic CO_2 since the mid-eighteenth century, resulting in an average 30% increase in global surface ocean acidity (AMAP, 2013; Pörtner et al., 2019; Sabine et al., 2004). The current understanding is that global mean surface acidification rates range from -0.027 to -0.016 pH_T units and -0.081 to -0.065 Ω_{Ar} units per decade since the 1980s (Iida et al., 2021; Lauvset et al., 2015; Ma et al., 2023; Orr et al., 2005; Pörtner et al., 2019). While this broad range is due in part to methodological differences and limited observational data, it primarily reflects the high spatial variability caused by diverse environmental factors impacting the carbonate system. In addition to anthropogenic CO_2 uptake, changes in temperature, salinity, or any of the carbonate system parameters can affect OA rates. While carbon uptake exclusively drives acidification, the effects of other processes may be less straightforward. For example, warming tends to decrease pH_T but increase Ω_{Ar} by promoting the dissociation of bicarbonate to carbonate (increasing $[CO_3^{2-}]$ and $[H^+]_F$). Additionally, warming also lowers CO_2 solubility, leading to CO_2 outgassing that further increases $[CO_3^{2-}]$ and decreases $[H^+]_F$ (Jiang et al., 2019; Xue et al., 2020).

Certain regions, such as coastal and high-latitude waters, exhibit acidification rates that significantly diverge from the global mean due to natural and anthropogenic processes not present in typical open-ocean environments. In addition to spatial variations in temperature, salinity, and carbonate system parameters, the influence of sea ice, watershed and riverine discharge, nutrient influx, and dense biological communities also drive variability in the marine carbonate system (Carstensen & Duarte, 2019; Duarte et al., 2013). Climate change has the potential to affect these processes and drive or offset OA, particularly in the dynamic Pacific-Arctic Region (PAR).

The PAR, as defined in this study, encompasses the west Arctic Ocean, its marginal seas (East Siberian, Chukchi, Beaufort), the western Canadian Archipelago, the Bering Sea, the Gulf of Alaska, and the subarctic Pacific Ocean (Figure 1). The PAR is highly vulnerable to OA due to its inherently low buffer capacity and $[CO_3^{2-}]$. This primes the PAR to absorb CO_2 as atmospheric concentrations rise, threatening to lower its already near-undersaturated Ω_{Ar} levels. The PAR's natural vulnerability, coupled with regional climate change impacts (H. Lee et al., 2023; Pörtner et al., 2019), have manifested in the highest observed rates of OA globally, with current trends suggesting it will be the first major body of water to reach complete surface undersaturation (AMAP, 2013, 2018; Fabry et al., 2009). At the same time, the region is gaining economic and geopolitical significance due to enhanced vessel accessibility resulting from reduced sea ice (Intergovernmental Panel on Climate Change (IPCC), 2023). Consequently, it is emerging as an economic hub in part due to its highly productive fisheries (IPCC, 2023). However, acidification may threaten to curb the region's fishery potential given its detrimental effects on marine calcifiers and their vital role in the food chain, underscoring the importance of quantifying regional acidification trends.

While numerous studies have documented surface pCO_2 dynamics (Bates, 2006; L. Chen & Gao, 2007; Cai et al., 2010; DeGrandpre et al., 2020; Ouyang et al., 2020, 2021; Tu et al., 2021; Wang et al., 2022a; Woosley & Millero, 2020) and episodic Ω_{Ar} undersaturation events (Chierici & Fransson, 2009; Robbins et al., 2013; Semiletov et al., 2016; Wynn et al., 2016; Yamamoto-Kawai et al., 2009; Mathis et al., 2012) in the PAR, research

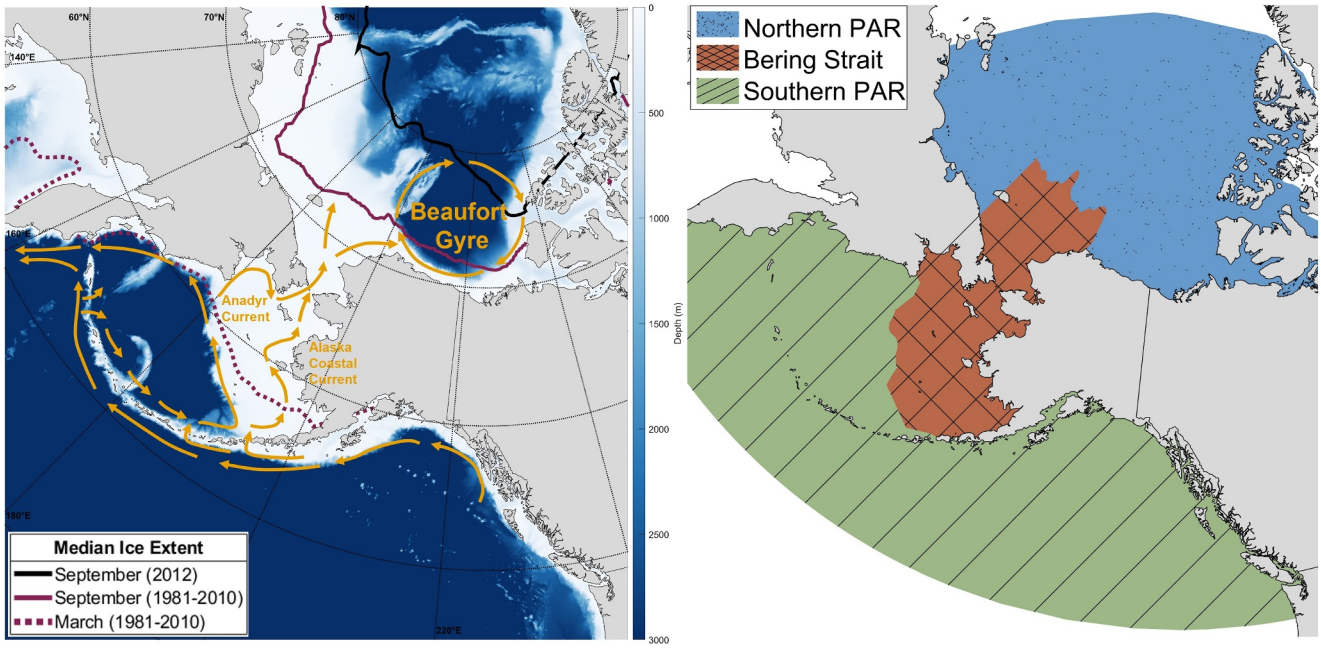

Figure 1. The Pacific-Arctic Region (PAR). (Left) Bathymetry is sourced from the General Bathymetric Chart of the Oceans (GEBCO 2023), ice extents from the National Snow and Ice Data Center. (Right) The PAR divided into three oceanographically similar subregions based on the Marine Ecoregions of the World (Spalding et al., 2007).

quantifying long-term (*i.e.*, decadal) carbonate system trends remain scarce. Table 1 lists the studies that have quantified surface rates for pCO_2, pH_T, and Ω_{Ar} and reveals a broad spectrum of results: 7.4 to 61.8 µatm pCO_2, −0.086 to −0.013 pH_T units, and −0.50 to −0.04 Ω_{Ar} units per decade (dec^{-1}). This wide range in trend values in Table 1 highlights two other important factors. For one, observational studies that quantify decadal acidification rates are notably limited. This scarcity primarily stems from the limited availability of direct carbonate system measurements in the PAR prior to the 1990s, and is further aggravated by significant spatial and temporal gaps within existing data. Second, observational studies that are available tend to concentrate on specific areas within the PAR, not the entire region. This focus is largely dictated by data availability, with regions such the Bering, Beaufort, and Chukchi Seas sampled more often than less accessible areas such as the East Siberian Sea or Canadian Archipelago. Furthermore, the variation in trend methodology and mechanism analysis across studies complicates direct trend comparisons between them. This study aims to address these gaps in our current understanding by applying a consistent trend methodology for the same time period across the entire study area.

2. Study Area

This study divided the PAR into three oceanographically similar subregions based on the Marine Ecoregions of the World (Spalding et al., 2007): the Southern PAR, the Bering Strait, and the Northern PAR (Figure 1). The Southern PAR is a deep-water, open-ocean, and typically ice-free environment comprised by the North Pacific ocean, Gulf of Alaska, and Bering Sea basin. Waters from the Southern PAR feed into the Northern PAR by passing through the Bering Strait. The Bering Strait subregion is composed of the shallow (<150 m depth) Bering Sea and Chukchi Sea continental shelves which are separated by the narrow (80 km wide) Bering Strait passage. This influx consists of saline, nutrient-rich Anadyr water from the Russian coast on the western sector of the PAR and fresher, lower-nutrient Alaskan Coastal water from the Alaskan coast on the eastern sector of the PAR (Grebmeier, 2012). These currents converge near the Bering Strait passage, driving primary productivity in one of the world's most productive marine ecosystems (Grebmeier, 2012; Grebmeier et al., 2006).

The high primary productivity observed in the Bering Strait subregion is closely tied to its seasonal sea ice dynamics. Sea ice extent is typically at its highest in March and lowest in September. Figure 1 depicts the median March and September ice extent for the years 1981–2010. Waters between the March and September ice extents (*i.e.*, the Bering Strait subregion) undergo seasonal changes in ice coverage. Areas south of the March extent are

Table 1
Published Studies That Report Pacific-Arctic Region Surface Trends in pCO_2, pH_T, And/Or Ω_{Ar}

Reference	Subregion	Time span	pCO_2 rate	pH_T rate	Ω_{Ar} rate	Note
Observation-based						
Ma et al. (2023)	Southern PAR	1982–2021	15.9	−0.017	−0.048	NP-SPSS (Figure 3)
Lauvset et al. (2015)	Southern PAR	1991–2011	7.4	−0.013	–	NP-SPSS (Figure 1)
Ouyang et al. (2020)	Northern PAR	1994–2017	46.0	–	–	Canada Basin (Figure 1)
Ouyang et al. (2020)	Northern PAR	1994–2017	38.1	–	–	Beaufort Sea (Figure 1)
Qi et al. (2022)	Northern PAR	1994–2020	–	−0.086 to −0.031	−0.20 to −0.11	IC, NWCB, NECB, SCB (Figure 1a)
Zhang, Yamamoto-Kawai, and Williams (2020)	Northern PAR	1997–2007	–	–	−0.50	
Zhang, Yamamoto-Kawai, and Williams (2020)	Northern PAR	2007–2016	–	–	No Trend	
Model Output						
Mathis et al. (2015)	Bering Strait	2011–2100	–	–	−0.07	
Mathis et al. (2015)	Bering Strait	2011–2100	–	–	−0.06	
Mathis et al. (2015)	Northern PAR	2011–2100	–	–	−0.06	
Pilcher et al. (2019)	Bering Strait	2003–2012	–	–	−0.40 to −0.25	
Pilcher et al. (2022)	Bering Strait	2010–2100	17.5 to 61.8	−0.045 to −0.015	−0.10 to 0.04	
Mortenson et al. (2020)	Northern PAR	1981–2015	21.3	−0.03	−0.04	Beaufort Shelf (Figure 1b)
Mortenson et al. (2020)	Northern PAR	1981–2015	12.6	−0.02	−0.05	Beaufort Basin (Figure 1b)
Mortenson et al. (2020)	Northern PAR	1981–2015	19.6	−0.03	−0.09	CPS (Figure 1b)
Gruber et al. (2012)	Northern PAR	1935–2064	–	–	−0.07	Approx. from Figure 3

Note. pCO_2, pH_T, and Ω_{Ar} trends are in µatm dec^{-1}, pH_T units dec^{-1}, and Ω_{Ar} units dec^{-1}, respectively. Studies are categorized as observation-based or model output. Observation-based means trends were derived from direct observations or on algorithmically predicted data (*e.g.*, neural network). The subregion column refers to the closest-matching area from Figure 1. Figures listed in the notes column refer to figures from that publication.

generally ice-free throughout the year, while regions north of the September line maintain year-round ice cover. Sea ice breakup and melting in the Bering Strait subregion drive spring phytoplankton blooms by allowing more light to penetrate the water column and keeping nutrients at the surface through increased stratification (Grebmeier, 2012). Declining sea ice coverage has lengthened the growing season and led to the emergence of fall phytoplankton blooms. These blooms are facilitated by extended light availability due to ice forming later in the season and the replenishment of surface nutrients through storm-induced upwelling (Waga & Hirawake, 2020). The cold, highly soluble water of the region combined with high primary productivity makes the Bering Strait subregion an exceptionally strong CO_2 sink.

North of the Bering Strait, surface circulation in the Northern PAR is dominated by the Beaufort Gyre. Situated between the continental shelves of the Chukchi Sea, Beaufort Sea, and Canadian Archipelago, the Beaufort Gyre is a clockwise-rotating surface circulation system that lies over the deepwater (mean depth 3.8 km) Canada Basin. The Beaufort Gyre is the largest freshwater reservoir in the Arctic. It contains approximately 25% of the Arctic Ocean's total freshwater due to freshwater discharge from Russian and North American rivers and, in recent decades, significant sea ice loss (Timmermans & Toole, 2023). Climate change-driven warming has caused significant sea ice decline in the Arctic (Chapman & Walsh, 1993; Kwok, 2018; Walsh & Chapman, 2001). This loss is particularly rapid in the Northern PAR, with the Beaufort Gyre and nearby marginal seas exhibiting a sea ice cover decline of 10%–30% per decade since 1979 (Timmermans & Toole, 2023). This is illustrated by the September 2012 ice extent (Figure 1), the lowest extent on record (Timmermans & Toole, 2023), which is significantly further north than the median September ice extent of the prior three decades.

Table 2
Gridded Data Sets Used in This Study

Data set	Spatial resolution	Temporal resolution	Variables used	Uncertainty included	Methodology	Reference
Data sets used for analysis						
SOM-FFN (v2024)	1° × 1°	Monthly	pCO_2, air-sea C flux	No	Neural network	Jersild et al. (2017)
Hadley EN4 (EN.4.2.2)	1° × 1°	Monthly	SSS	Yes	Objective analysis	Good et al. (2013)
OI SST (v2)	1° × 1°	Monthly	SST	Yes	Objective analysis	Reynolds et al. (2002)
WOA 2018	1° × 1°	Monthly[a]	Si, PO_4^{3-}	No	Objective analysis	Garcia et al. (2019)
Data sets used for validation and comparison						
OceanSODA-ETHZ (v2023)	1° × 1°	Monthly	pCO_2, pH_T, Ω_{Ar}	Yes	Neural network	Gregor and Gruber (2021)
CMEMS-LSCE (r100)	1° × 1°	Monthly	pCO_2, pH_T, Ω_{Ar}	Yes	Neural network	Chau et al. (2023)
CMEMS-LSCE (r25)	0.25° × 0.25°	Monthly	pCO_2, pH_T, Ω_{Ar}	Yes	Neural network	Chau et al. (2023)
SOCAT (v2024)	1° × 1°	Monthly	fCO_2	Yes	Observational	Bakker et al. (2016)
ORAS5	0.25° × 0.25°	Monthly	Sea ice thickness	No	Reanalysis	Zuo et al. (2019)

[a]WOA silicate and phosphate data are a monthly climatology.

3. Methods

Discrete Bottle Sample Data sets. To quantify carbonate system trends, we began by compiling a comprehensive data set of field samples. These samples were used to train TA prediction models, validate carbonate system predictions, and propagate uncertainties to the final trend calculations. Discrete bottle samples were primarily sourced from the Global Ocean Data Analysis Project, GLODAPv2.2023 (Lauvset et al., 2024), due to its extensive data coverage and rigorous quality control. The data set was expanded by leveraging online databases and individual publications. Only observations in the upper 10 m with a WOCE quality flag of 2 consisting of SSS, SST, depth, and at least one carbonate system parameter were selected. Details regarding the utilized data sets, data standardization, and quality control measures are provided in Figure S1 and Text S1 in Supporting Information S1, and Table S1.

Gridded Data sets. Gridded data sets complemented discrete bottle samples by providing broader spatial and temporal coverage. The data sets used in this study, listed in Table 2, have a monthly resolution and span January 1993 to December 2021. Although some data sets include earlier data, the scarcity of carbonate system sampling in the PAR before the 1990s (Figure S1 in Supporting Information S1) led us to restrict the study period to ensure sufficient field measurements for validation.

Two carbonate system variables are necessary to resolve the full carbonate system. While we produced our own gridded TA data set, we utilized the SOM-FFN (v2024) pCO_2 data set for the second carbonate system variable. The SOM-FFN pCO_2 data set is the output of a two-step neural network, detailed and validated in previous works (Landschützer et al., 2013, 2014, 2016), and expanded in 2023 to encompass the Arctic Ocean. This approach categorizes the global ocean into biogeochemically similar regions using a self-organizing map, then leverages a feed-forward neural network (FFN) to establish regional non-linear relationships between environmental variables (SSS, SST, atmospheric dry air CO_2 mixing ratio, mixed-layer depth, chlorophyll *a*) and surface pCO_2 observations from the Surface Ocean CO_2 Atlas (SOCAT). These relationships were applied to environmental parameter data sets, which offer broader spatial and temporal coverage than direct surface pCO_2 measurements, to produce a monthly gapless gridded surface pCO_2 data set. The OceanSODA-ETHZ and CMEMS-LSCE data sets similarly use neural network methods but predict the entire carbonate system rather than just pCO_2. The SOM-FFN pCO_2 data set was selected as our second carbonate system variable because it is the only data set from Table 2 with complete spatial and temporal coverage of the Arctic Ocean.

Carbonate System Reconstruction. The carbonate system reconstruction process is outlined in Figure 2a. Using Equation 1, we employed SSS and SST as predictor variables to predict TA with a geographically weighted regression (GWR) model trained on 7,148 TA samples from the upper 10 m across the PAR.

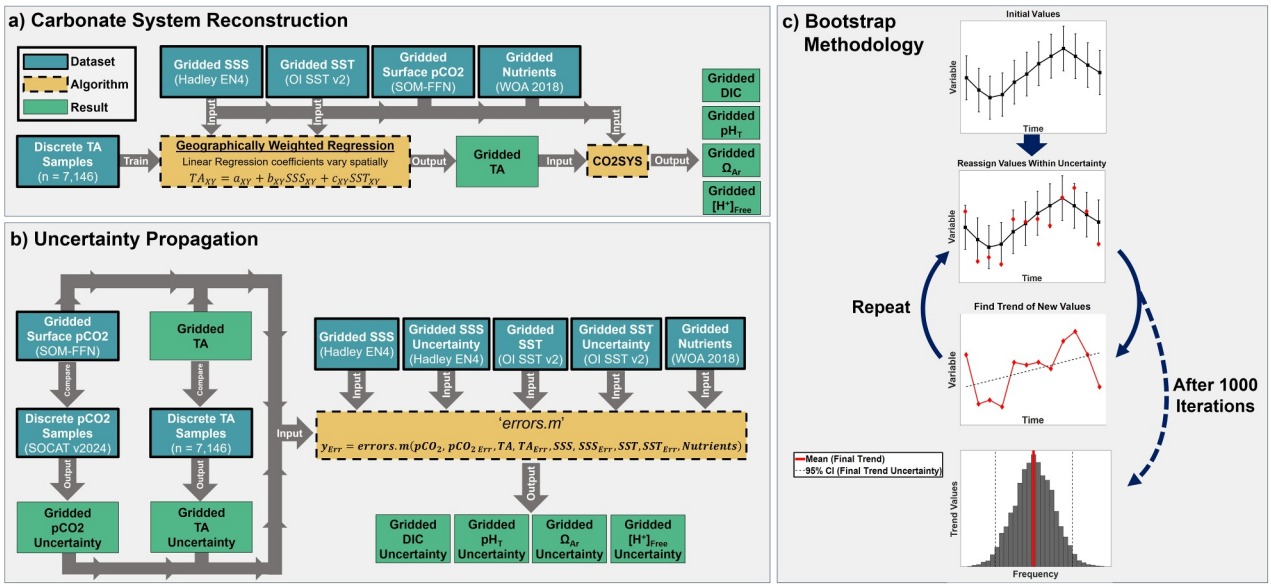

Figure 2. Methods flowchart. (a) Discrete Total alkalinity (TA) samples trained a geographically weighted regression model, which, combined with gridded SSS and SST, produced a gridded TA data set. Gridded SSS, SST, pCO_2, TA, and nutrient data sets were input into CO2SYS to solve the remaining carbonate system. (b) Uncertainty fields for pCO_2 and TA were generated by comparing discrete samples to gridded data sets; SSS and SST uncertainties were pre-existing. These data sets and their uncertainties (excluding nutrient uncertainty) were processed through the CO2SYS "errors.m" subroutine to derive carbonate system uncertainty fields. (c) Trend uncertainties were calculated by propagating monthly value uncertainties via a bootstrap method: each monthly value (black square) was randomly reassigned a new value (red diamond) within its uncertainty range (error bars). This was repeated 1,000 times, each time finding the trend with the Theil-Sen slope estimator, to generate a distribution of trends. The mean and 95% confidence interval of this distribution represent the final trend and its uncertainty.

$$\mathrm{TA} = a + b(\mathrm{SSS}) + c(\mathrm{SST}) \tag{1}$$

GWR is a variant of ordinary least squares linear regression that allows coefficients to vary spatially. In essence, GWR performs a linear regression at each observation point and weights neighboring observations by their distance, with closer observations carrying more weight. This produces unique intercept (a) and slope (b and c) values for each TA sample location, which can then be averaged onto a continuous two-dimensional grid and interpolated in grid cells lacking TA samples. GWR was implemented using the MATLAB Spatial Econometrics Toolbox (LeSage, 1999). All GWR calculations were conducted in a polar stereographic projection to ensure uniform grid cell areas and avoid spatial distortion at high latitudes. Final results were then converted back to a 1° × 1° grid. This step was particularly important as the study area spans a broad latitudinal range (45°–90°N).

The trained GWR model was applied to gridded SSS and SST data sets to produce a gridded TA data set. CO2SYSv3 (Lewis & Wallace, 1998) for MATLAB (van Heuven et al., 2011) was then used with the gridded TA, pCO_2, SSS, SST, silicate, and phosphate data sets to calculate monthly averaged 1° × 1° DIC, pH_T, $[H^+]_F$, and Ω_{Ar} fields. We report pH on the total scale (pH_T), as recommended by OA best practices (Dickson, 2007; Riebesell et al., 2011). Conversely, hydrogen ion concentration is reported on the free scale ($[H^+]_F$), which excludes sulfate ions and is more relevant when considering biological impacts (Ma et al., 2023). K_1 and K_2 dissociation constants of Mehrbach et al. (1973) as refit by Dickson and Millero (1987) were selected as they show the greatest internal consistency compared to other constants in the Arctic and yield the lowest error when TA and pCO_2 are used as input variables (Chen et al., 2015; Raimondi et al., 2019). All other constants were the default/recommended CO2SYS settings: K_{SO4} dissociation constants from Dickson (1990) and the boron/chlorinity ratio from Uppström (1974).

Carbonate System Uncertainty. The validity of final trend results depends on the accuracy of the reconstructed carbonate system. Therefore, error was meticulously propagated through to the final trends and drivers. The uncertainty propagation methodology for carbonate system predictions is outlined in Figure 2b. The SOM-FFN pCO_2 data set did not include gridded uncertainty values. Although the method demonstrates near-zero bias and <20 µatm RMSE globally (Landschützer et al., 2016), its effectiveness in the Arctic Ocean and at a 1° × 1° spatial

resolution has not been evaluated in the literature. To account for this, we compared the gridded pCO_2 data to SOCAT v2024, averaged the residuals onto a $1° \times 1°$ grid, and interpolated spatial gaps to create a gapless $1° \times 1°$ pCO_2 uncertainty field. Gridded TA uncertainty was calculated in the same manner using residuals from the GWR TA prediction model. Error was assessed using mean absolute error $\left(\text{MAE} = \frac{\Sigma \left| y_{\text{Pred}} - y_{\text{Obs}} \right|}{N_{\text{Obs}}}\right)$ and mean bias error $\left(\text{MBE} = \frac{\Sigma \left(y_{\text{Pred}} - y_{\text{Obs}} \right)}{N_{\text{Obs}}}\right)$.

We assumed pCO_2 and TA uncertainty was consistent over time due to insufficient spatiotemporal data coverage to support time-dependent uncertainty fields, though recent evidence suggests the SOM-FFN product does exhibit seasonal patterns in uncertainty (Jersild & Landschützer, 2024). Error was propagated from the derived pCO_2 and TA uncertainty fields to calculated carbonate system variables (DIC, pH_T, $[H^+]_F$, Ω_{Ar}) using the CO2SYS "errors.m" subroutine (Orr et al., 2018). Although uncertainty (u) in our calculated carbonate system variables is heavily influenced by the uncertainty in pCO_2 (u_{pCO2}) and TA (u_{TA}), it also depends on the state of the carbonate system (*i.e.*, the values of pCO_2, TA, SSS, SST, Si, and PO_4^{3-}) per Equation 2, as well as the uncertainty of dissociation constants. This introduces both spatial and seasonal variability to the uncertainty of calculated variables, as detailed further in Text S2.

$$u_{\text{DIC},pH_T,[H^+]_F,\Omega_{Ar}} = \text{errors.m}\left(pCO_2, u_{pCO2}, \text{TA}, u_{\text{TA}}, \text{SSS}, u_{\text{SSS}}, \text{SST}, u_{\text{SST}}, \text{Si}, PO_4^{3-}\right) \quad (2)$$

Statistical Trend Methods. Once the carbonate system was reconstructed, we applied statistical trend methods to determine carbonate system variable rates. However, detecting and quantifying trends in the marine carbonate system requires careful consideration due to its non-linear response to external influences such as increasing atmospheric CO_2 and concurrent climate change-driven impacts on DIC, TA, SSS, and SST. This task is further nuanced by inherent seasonality in oceanographic variables, meaning a robust statistical approach is more suitable than simple linear regression. Therefore, we utilized the seasonal Kendall trend test and Theil-Sen slope estimator for trend analysis in this study.

The seasonal Kendall trend test (Hirsch et al., 1982), a non-parametric (*i.e.*, distribution-free) method, excels in identifying both the presence and direction of monotonic trends in seasonal data. This test determines whether there is an upward or downward trend between every possible pair of data points. When no overall trend exists, the total number of upward and downward trends between all pairs should be approximately equal. In contrast, an underlying trend would yield more pairwise trends in one direction than could be explained by random chance. Seasonality is handled by only comparing data points within the same month, then integrating individual monthly statistics into a single overall trend.

While the seasonal Kendall trend test identifies trend direction in seasonal data, it does not measure trend magnitude. This limitation is addressed by the seasonal Theil-Sen estimator (Sen, 1968). Similar to the seasonal Kendall Trend test, this non-parametric method quantifies trend magnitude by first finding the slopes between all pairs of data points with the same month (*e.g.*, all June values of a time series). This produces a distribution of slope values, the median of which is the trend value for that month. Repeating this process for every month of the year yields 12 slope values, the median of which is the overall trend.

The seasonal Kendall trend test and Theil-Sen estimator are widely used in environmental trend analysis. This combined approach has been extensively applied to study long-term trends in environmental parameters such as salinity (Wiseman et al., 1990), chemical concentrations (Lehmann et al., 2005; R. A. Smith et al., 1982), aquatic heatwaves (Kaushal et al., 2010; Tassone et al., 2021, 2023), sea-level rise (Nguyen et al., 2022; Taibi & Haddad, 2019), and phytoplankton blooms (Friedland et al., 2018).

The uncertainty of carbonate system predictions was accounted for in the overall trend by utilizing a bootstrap approach, as shown in Figure 2c. Bootstrapping the seasonal Kendall trend test involved re-assigning each monthly mean in every grid cell a random value within its uncertainty range before conducting the test. Repeating this procedure 1,000 times yielded a normally distributed set of 1,000 p-values and trend directions at every grid cell. A grid cell's trend direction was deemed statistically significant if at least 95% of the bootstrapped p-values were below 0.05 with a consistent trend direction.

Trend magnitude and uncertainty was calculated using a similar approach: every monthly mean at every grid cell was re-assigned a random value within its uncertainty range, then the slope of each grid cell's time series was computed using the seasonal Theil-Sen estimator. Repeating 1,000 times yielded a normally distributed set of 1,000 slopes for each grid cell, the mean of which was used as the trend magnitude and the 95% confidence interval the trend uncertainty.

Driver Decomposition. Once carbonate system trends were determined, Ω_{Ar} and $[H^+]_F$ trends were decomposed into individual drivers to reveal which processes drove or mitigated observed acidification trends. This decomposition approach was modeled after the work of Ma et al. (2023). A discrete change in a calculated carbonate system parameter (y) is caused by changes in its drivers (X) relative to the sensitivity of y to these changes ($\delta y/\delta X$). This is represented by the first-order terms of a Taylor expansion (Landschützer et al., 2018; Takahashi et al., 1993) given by Equation 3. The drivers (X) were salinity-normalized TA and DIC (sTA and sDIC), freshwater (FW), and SST. Normalizing TA and DIC to a constant salinity removed the effects of freshwater additions (which dilute TA and DIC) or removals (which concentrate TA and DIC). The FW term accounts for changes in SSS and the associated effects on TA and DIC ($FW = FW_{SSS} + FW_{TA} + FW_{DIC}$). FW_{TA} and FW_{DIC} were calculated by taking the difference between trends in TA and sTA, and DIC and sDIC, respectively, while FW_{SSS} represents SSS directly. Nutrients were omitted as drivers because climatological values lack long-term trends, though their values were used in sensitivity calculations.

$$\Delta y = \sum_{X\,=\,sTA,sDIC,FW,SST} \left(\frac{\delta y}{\delta X} \cdot \Delta X \right) \tag{3}$$

To compare the impact of changing drivers and sensitivities across subregions with different baseline Ω_{Ar} and $[H^+]_F$ values, we replaced the sensitivity term in Equation 3 with relative sensitivities (ω_X and β_X) given by Equations 4 and 5.

$$\omega_X = \frac{1}{\Omega_{Ar}} \cdot \frac{\delta \Omega_{Ar}}{\delta X} \tag{4}$$

$$\beta_X = \frac{1}{[H^+]_F} \cdot \frac{\delta [H^+]_F}{\delta X} \tag{5}$$

Replacing the sensitivities in Equation 3 with the relative sensitivities of Equations 4 and 5 results in the updated Taylor expansions given by Equations 6 and 7. Note that, in order to maintain proper units and account for the added $1/\Omega_{Ar}$ and $1/[H^+]_F$ terms, we must multiply each term by Ω_{Ar} and $[H^+]_F$, respectively (*i.e.*, $1/\Omega_{Ar} \cdot \Omega_{Ar}$ cancel, maintaining the equality in Equations 6 and 7).

$$\Delta \Omega_{Ar} = \sum_{X\,=\,sTA,sDIC,FW,SST} (\omega_X \cdot \Omega_{Ar} \cdot \Delta X) \tag{6}$$

$$\Delta [H^+]_F = \sum_{X\,=\,sTA,sDIC,FW,SST} (\beta_X \cdot [H^+]_F \cdot \Delta X) \tag{7}$$

The same concept holds true for trends: a trend in y must be due to trends in its drivers and/or sensitivities. Taking the derivative of Equations 6 and 7 with respect to time using the product rule gives the total trends in Ω_{Ar} (Equation 8) and $[H^+]_F$ (Equation 9), where X = sTA, sDIC, FW, and SST.

$$\frac{d\Omega_{Ar}}{dt} = \sum_X \left(\underbrace{\frac{d\omega_X}{dt} \cdot \overline{\Omega}_{Ar} \cdot \Delta X}_{\text{change in sensitivity}} + \underbrace{\overline{\omega}_X \cdot \frac{d\Omega_{Ar}}{dt} \cdot \Delta X}_{\text{mass effect}} + \underbrace{\overline{\omega}_X \cdot \overline{\Omega}_{Ar} \cdot \frac{d\Delta X}{dt}}_{\text{change in driver}} \right) \tag{8}$$

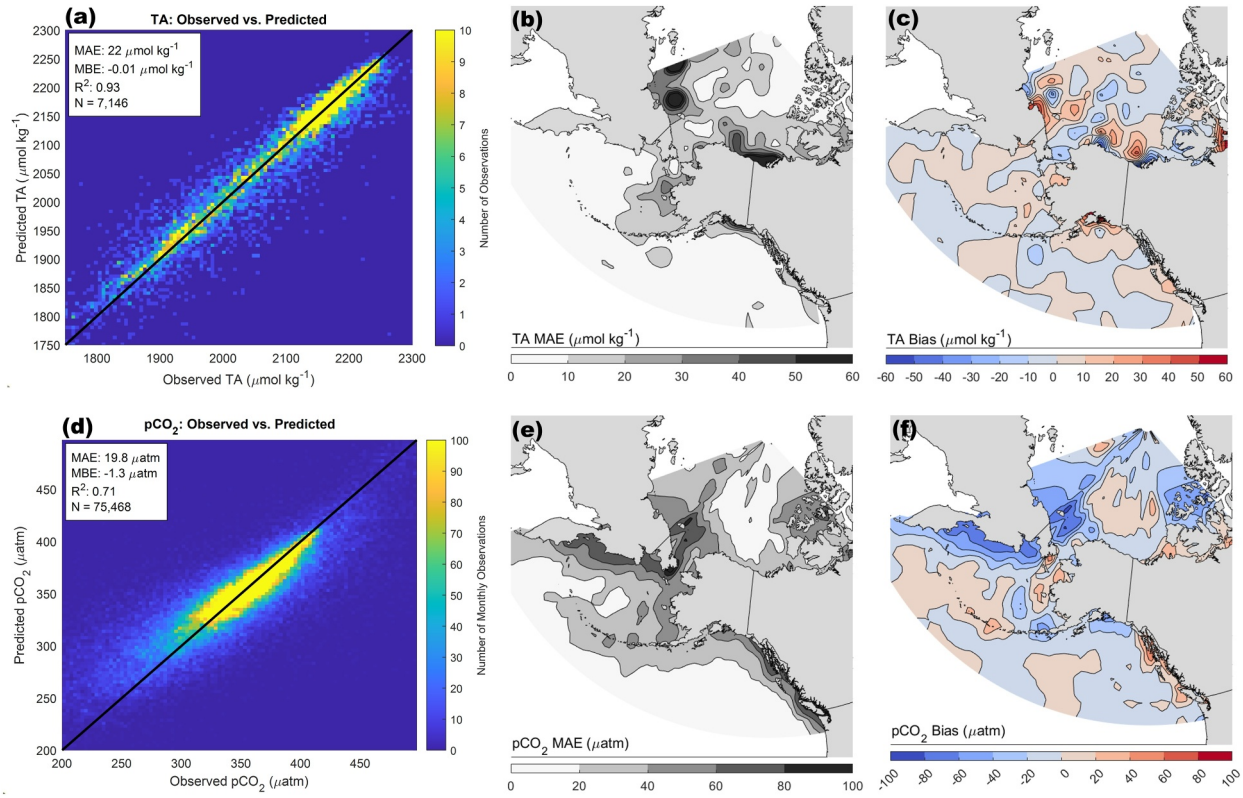

Figure 3. Total alkalinity (TA) prediction statistics for the entire Pacific-Arctic Region (PAR) (a), along with the spatial distribution of error (b), and bias (c). Similarly, pCO_2 prediction statistics for the entire PAR are shown (d), with the spatial distribution of error (e) and bias (f). Note that (b) and (e) represent the TA and pCO_2 uncertainty fields used in error propagation. The color scale of (a) and (d) denote data density, with yellow indicating more data points.

$$\frac{d[H^+]_F}{dt} = \sum_X \left(\underbrace{\frac{d\beta_X}{dt} \cdot \overline{[H^+]_F} \cdot \Delta X}_{\text{change in sensitivity}} + \underbrace{\overline{\beta_X} \cdot \frac{d[H^+]_F}{dt} \cdot \Delta X}_{\text{mass effect}} + \underbrace{\overline{\beta_X} \cdot \overline{[H^+]_F} \cdot \frac{d\Delta X}{dt}}_{\text{change in driver}} \right) \quad (9)$$

Sensitivities were calculated for each grid cell by inputting long-term averages of DIC, TA, SSS, SST, silicate, and phosphate fields into the CO2SYS "derivnum" subroutine. ΔX is the discrete change in driver from 1993 to 2021. All time derivatives were calculated using the seasonal Theil-Sen estimator except for $d\Delta X/dt$, which was calculated by dividing ΔX by 29 years. Variables denoted by a bar on top indicate the long-term mean for the grid cell. This decomposition yields three distinct terms for each driver: change in sensitivity, mass effect, and change in the driver itself, the sum of which equals the contribution of that driver to the total trend in Ω_{Ar} or $[H^+]_F$. The sum of all three terms across all four drivers equals the total trend.

Salinity Normalization. TA and DIC were normalized to a constant salinity of 34.5 psu using Equations 10 and 11 (Friis et al., 2003). The linear relationships between SSS and TA, and SSS and DIC, vary by location due to processes such as sea-ice formation and melting, upwelling, surface water mass exchange, calcification, and primary production (Friis et al., 2003). This variability highlights why a GWR approach was significantly more effective at predicting TA than applying a single set of regression coefficients across the entire PAR. Consequently, spatially variable zero-salinity TA ($TA_{SSS=0}$) and DIC ($DIC_{SSS=0}$) values (*i.e.*, the intercepts of local linear regressions) must be considered when normalizing to a constant salinity. $TA_{SSS=0}$ and $DIC_{SSS=0}$ are gridded GWR intercept fields calculated by running independent GWRs where TA and DIC are functions of salinity (*i.e.*, coefficient a in equations $TA = a + b(SSS)$ and $DIC = a + b(SSS)$, respectively).

$$sTA = \frac{TA - TA_{SSS=0}}{SSS} \cdot 34.5 + TA_{SSS=0} \quad (10)$$

$$sDIC = \frac{DIC - DIC_{SSS=0}}{SSS} \cdot 34.5 + DIC_{SSS=0} \quad (11)$$

4. Results

Carbonate System Reconstruction. Using GWR to predict TA with SSS and SST as predictor variables resulted in an R^2 of 0.93, MAE of 22 μmol kg^{-1}, and bias (MBE) of −0.01 μmol kg^{-1}, as shown in Figure 3a. SSS was the primary determinant of TA; however, the inclusion of SST improved prediction accuracy in specific areas. For instance, regions experiencing seasonal shifts in water masses may benefit from the SST term, as water masses are identified by both temperature and salinity. Additionally, temperature-driven processes such as primary productivity, sea ice melt, and riverine discharge influence TA, which the SST term may partially account for.

The spatial distributions of TA uncertainty (MAE) and bias (MBE), shown in Figures 3b and 3c, provide a more nuanced perspective than the aggregate statistics in Figure 3a. While the overall TA MAE is 22 μmol kg^{-1}, 72% of the study region (by area) exhibited a TA MAE below 20 μmol kg^{-1}. However, highly localized coastal areas in the Beaufort and East Siberian Sea exhibited TA MAE values as high as 60 μmol kg^{-1}, raising the overall average. While bias was consistently low and did not favor a particular direction across the region, the same coastal areas with high TA MAE also exhibited bias as large as ±40 μmol kg^{-1}, significantly higher than the overall TA MBE of −0.1 μmol kg^{-1} may suggest.

Comparison of the SOM-FFN surface pCO_2 data set to in situ observations yielded an R^2 of 0.71, MAE of 19.8 μatm, and bias (MBE) of −1.3 μatm as shown in Figure 3d. Similar to TA, the pCO_2 MAE and MBE fields (Figures 3e and 3f) highlight the spatial variability of prediction accuracy and bias not captured in the overall averages. pCO_2 predictions exhibited low error (<20 μatm) and bias (<10 μatm) in open-ocean areas. Predictive error and bias generally increased in coastal waters (MAE 20–60 μatm, MBE 20–40 μatm) with areas such as the Russian and southeast Alaskan coast exhibiting errors and bias values as high as 80 μatm. pCO_2 uncertainty should be considered cautiously, however, given that we are comparing highly variable discrete pCO_2 measurements (which vary between 58 and 1,000 μatm) to monthly averaged 1° × 1° grid cells. Therefore, undersampling and sampling biases may result in overestimated error and bias.

The gridded uncertainty fields derived through error propagation ("errors.m") were independently validated using residuals from discrete DIC, pH_T, and Ω_{Ar} bottle samples that were not part of the reconstruction process. These residuals closely align with the gridded uncertainty estimates. Figures 4a–4c show the mean gridded uncertainty fields for DIC, pH_T, and Ω_{Ar}, calculated using the "errors.m" subroutine as outlined in the uncertainty propagation flowchart (Figure 2b). Below each plot, Figures 4d–4f present the residuals from comparisons between the discrete bottle sample measurements and the corresponding reconstructed gridded values.

The DIC comparison yielded a MAE of 30.5 μmol kg^{-1} (N = 22,742), closely matching the gridded uncertainty estimates. Similarly, the MAE for pH_T was 0.061 units (N = 7,352), and for Ω_{Ar} it was 0.31 units (N = 4,896), both of which align well with their respective gridded uncertainty fields. This agreement between the residuals of reconstructed and observed carbonate system variables and the independently propagated uncertainty fields reinforces the robustness of the error propagation methodology and the reliability of the resulting trend calculations.

Regional Trends. Figure 5 illustrates the seasonal Kendall trend test results for January 1993 to December 2021, with Figure 6 showing spatial trends in pCO_2, $[H^+]_F$, pH_T, and Ω_{Ar} for the same time period. pCO_2 trends are shown alongside acidification trends to provide additional context, as it is a key input variable in our calculations. These results indicate widespread surface acidification across the PAR characterized by rising $[H^+]_F$ and declining pH_T and Ω_{Ar}. The Bering Strait subregion is an exception as it exhibits portions with no trend in $[H^+]_F$, pH_T, and Ω_{Ar}. The other exception is a small portion of the Northern PAR, near the North Pole, which shows an increase in pH_T and Ω_{Ar}. Average carbonate system trends for each subregion are presented in Table 3.

Southern PAR Trends. The Southern PAR exhibited rates similar to global acidification trends: 0.32 nmol kg^{-1} dec^{-1} for $[H^+]_F$, −0.018 pH_T units dec^{-1}, and −0.063 Ω_{Ar} units dec^{-1}, which agrees with the established literature (Table 1). pCO_2 increased by 17.45 μatm dec^{-1}, while rising trends in DIC (7.20 μmol kg^{-1} dec^{-1}) and

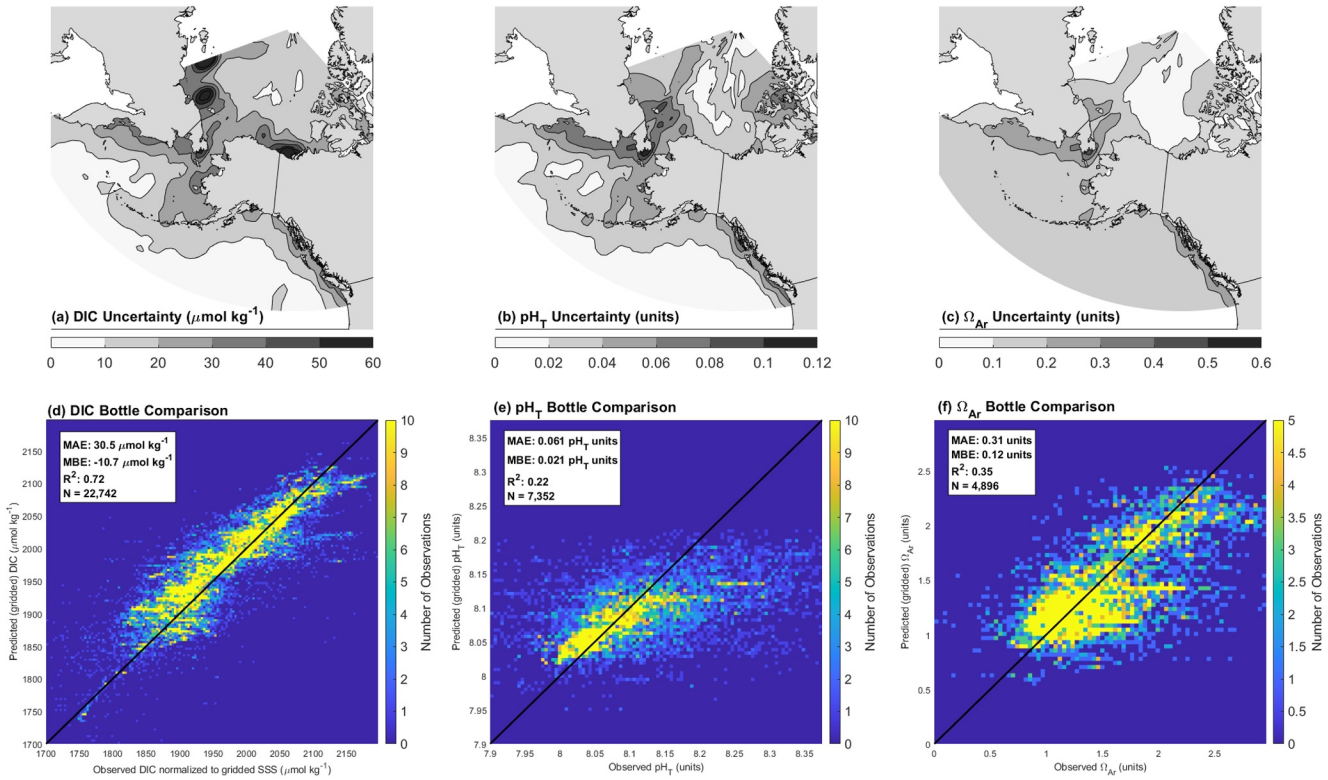

Figure 4. Propagated and observed uncertainty. (a–c) Gridded uncertainty fields for dissolved inorganic carbon (DIC), pH_T, and Ω_{Ar}, calculated using the "errors.m" subroutine as outlined in Figure 2b. These uncertainty fields, originally at a monthly resolution, were averaged over the entire study period to produce a single representative plot for each variable. (d–f) Residuals and corresponding statistics comparing discrete bottle sample measurements of DIC, pH_T, and Ω_{Ar} to the reconstructed gridded values. Notably, the results in panels (d–f) are independent of the propagated uncertainty fields in panels (a–c), as they are based on direct comparisons to discrete bottle samples not included in the reconstruction process. For DIC, the in situ salinity of the bottle samples was normalized to the gridded SSS value using Equation 11 to ensure an appropriate comparison.

sDIC (7.26 μmol kg^{-1} dec^{-1}) were indistinguishable within trend uncertainties of ±0.99 μmol kg^{-1} dec^{-1}, indicating freshwater addition/removal was minimal. This is highlighted by statistically insignificant trends in SSS (0.00 ± 0.01 psu dec^{-1}), TA (−0.13 ± 0.45 μmol kg^{-1} dec^{-1}), and sTA (−0.19 ± 0.41 μmol kg^{-1} dec^{-1}). The Southern PAR also exhibited a slight decrease in SST (−0.02 ± 0.02°C dec^{-1}).

Bering Strait Trends. Compared to global average trends, the Bering Strait subregion exhibited significantly lower rates for $[H^+]_F$ (0.18 nmol kg^{-1} dec^{-1}) and pH_T (−0.011 units dec^{-1}), as well as a near-zero trend for Ω_{Ar} (−0.020 ± 0.015 units dec^{-1}). Figures 5 and 6 show that, while the majority of the Bering Strait subregion had no trend in $[H^+]_F$, pH_T, or Ω_{Ar}, the eastern portion (off the Alaskan coast) did exhibit statistically significant acidification trends for these variables. Overall, the Bering Strait subregion exhibited a minor increase in pCO_2 (9.58 μatm dec^{-1}), DIC (2.71 μmol kg^{-1} dec^{-1}), and sDIC (2.48 μmol kg^{-1} dec^{-1}). There were no statistically significant overall trends for SSS (0.01 ± 0.05 psu dec^{-1}), TA (0.16 ± 1.31 μmol kg^{-1} dec^{-1}), or sTA (0.08 ± 1.19 μmol kg^{-1} dec^{-1}). The Bering Strait did exhibit the highest warming rate (0.05°C dec^{-1}) of the entire PAR.

Northern PAR Trends. The Northern PAR was characterized by the most pronounced acidification rates observed in this study with an average $[H^+]_F$ increase of 0.53 nmol kg^{-1} dec^{-1}, pH_T decrease of −0.028 units dec^{-1}, and an Ω_{Ar} rate of −0.078 units dec^{-1}. The Beaufort Gyre was the epicenter of this acidification, with surface rates 2–4 times higher than the global average: 1.16 nmol kg^{-1} dec^{-1} for $[H^+]_F$, −0.056 pH_T units dec^{-1}, and −0.180 Ω_{Ar} units dec^{-1} (Figure 6). While TA declined notably (−24.09 μmol kg^{-1} dec^{-1}), sTA was statistically insignificant (−0.63 ± 1.45 μmol kg^{-1} dec^{-1}). Likewise, we observed a substantial decrease in DIC (−14.87 μmol kg^{-1} dec^{-1}) which contrasted with rising pCO_2 (21.16 μatm dec^{-1}) and sDIC (6.94 μmol kg^{-1} dec^{-1}). The notable differences

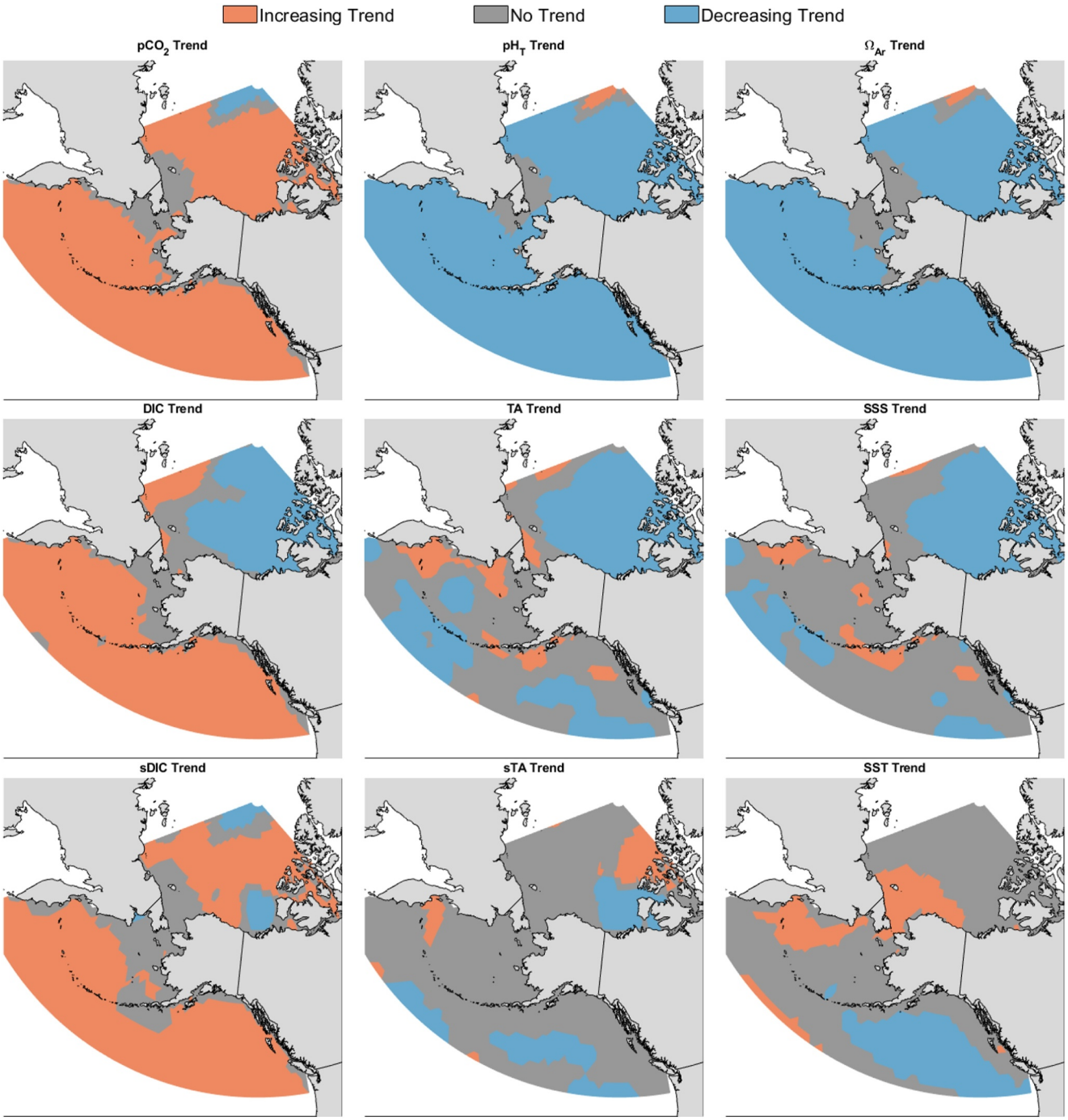

Figure 5. A seasonal Kendall trend test was conducted 1,000 times at each grid cell. Areas in orange (increasing trend) and blue (decreasing trend) had a positive and negative mean Mann-Kendall statistic, respectively, with more than 95% of bootstrapped p-values below 0.05. Gray (no trend) represents areas where <95% of the bootstrapped values had a p-value <0.05. This does not mean the result is statistically insignificant, but rather we failed to reject the null hypothesis of no trend. This means either the genuine absence of a trend or that the trend exists but is undetectable due to uncertainty. $[H^+]_F$ results are omitted as they mirror pH_T results.

between TA and sTA, and DIC and sDIC, indicate that freshwater addition played a significant role in carbonate system dynamics, which is further evidenced by substantial declines in SSS (-0.44 psu dec^{-1}). The Northern PAR exhibited slight signs of warming (0.03 ± 0.03°C dec^{-1}) but less than the Bering Strait subregion.

Ω_{Ar} and $[H^+]_F$ Drivers. The results of the driver decomposition, averaged by subregion, are presented in Figure 7. In all cases, changes in sensitivity and the mass effect had near-equal magnitudes and opposite directions,

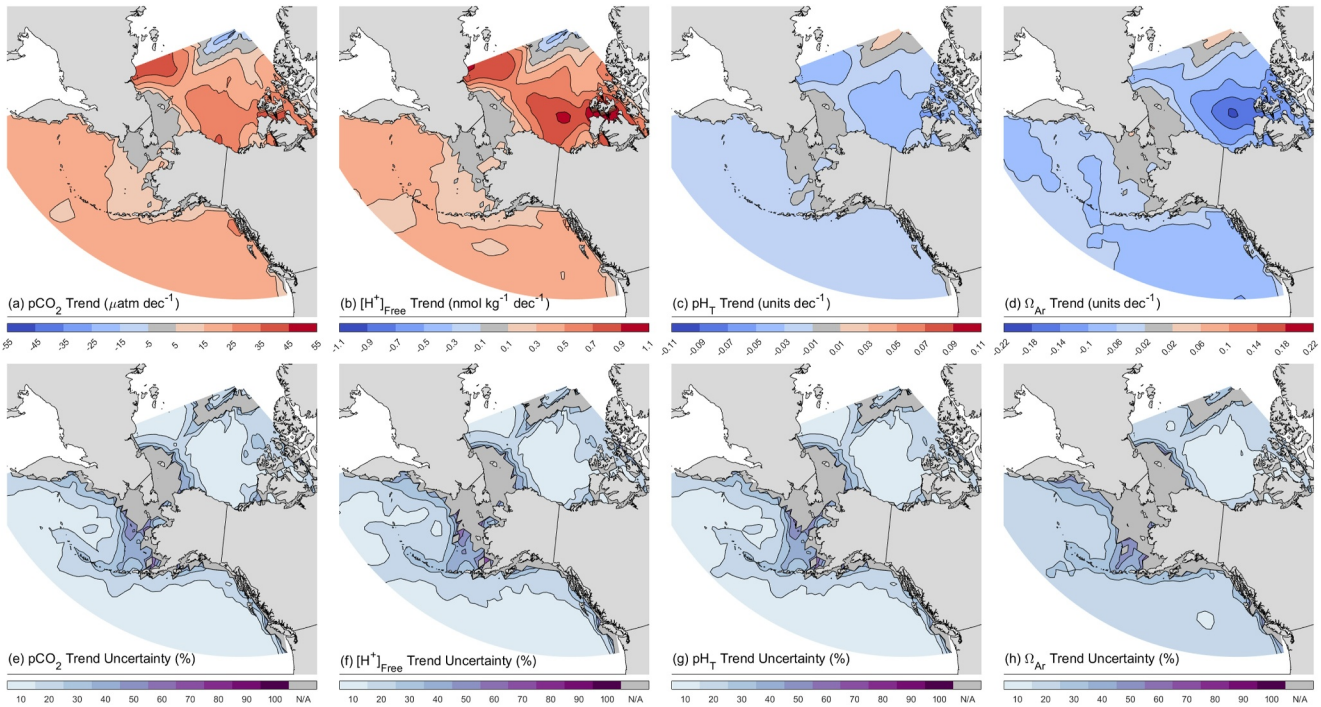

Figure 6. The decadal trend (1993–2021) and relative trend uncertainty for pCO_2, $[H^+]_F$, pH_T, and Ω_{Ar} determined via the bootstrapped seasonal Theil-Sen estimator approach. Gray denotes grid cells with no statistically significant trend (Figure 5).

meaning that changes in the drivers (sDIC, sTA, SST, FW) were solely responsible for long-term trends in Ω_{Ar} and $[H^+]_F$. As such, our results and discussion will focus solely on the change in driver's contribution to acidification trends. Each driver is presented in units of Ω_{Ar} units dec^{-1} or nmol H^+_{Free} kg^{-1} dec^{-1} to show how much the change in that driver contributed to the overall trend in Ω_{Ar} or $[H^+]_F$ (Equations 8 and 9). The sum of all the driver's contributions to these trends closely matches the overall trends of Table 3, but may not exactly match due to the inherent randomness of the bootstrap trend methodology. Figure 7 also includes individual components of the FW driver ($FW = FW_{SSS} + FW_{TA} + FW_{DIC}$) for additional context on freshwater effects. Specific values for

Table 3
Area-Weighted Average of Trends and Trend Uncertainties for Each Subregion From January 1993 to December 2021

	Southern PAR	Bering strait	Northern PAR	Units (dec^{-1})
pCO_2	17.45 ± 1.85	9.58 ± 3.87	21.16 ± 2.40	μatm
$[H^+]_{Free}$	0.32 ± 0.04	0.18 ± 0.09	0.53 ± 0.06	nmol kg^{-1}
pH_T	−0.018 ± 0.002	−0.011 ± 0.004	−0.028 ± 0.003	pH_T units
Ω_{Ar}	−0.063 ± 0.011	−0.020 ± 0.015	−0.078 ± 0.010	Ω_{Ar} units
DIC	7.20 ± 0.99	2.71 ± 2.01	−14.87 ± 1.93	μmol kg^{-1}
sDIC	7.26 ± 0.98	2.48 ± 2.04	6.94 ± 1.78	μmol kg^{-1}
TA	−0.13 ± 0.45	0.16 ± 1.31	−24.09 ± 1.70	μmol kg^{-1}
sTA	−0.19 ± 0.41	0.08 ± 1.19	−0.63 ± 1.45	μmol kg^{-1}
SSS	0.00 ± 0.01	0.01 ± 0.05	−0.44 ± 0.07	psu
SST	−0.02 ± 0.02	0.05 ± 0.02	0.03 ± 0.03	°C

Note. For each variable, every grid cell has a distinct trend and trend uncertainty calculated via the bootstrap method. The mean trend for each subregion was derived by computing the area-weighted average of all grid cell trend values within the subregion. The trend uncertainty for each subregion was calculated by taking the area-weighted average of all grid cell trend uncertainty values within the zone.

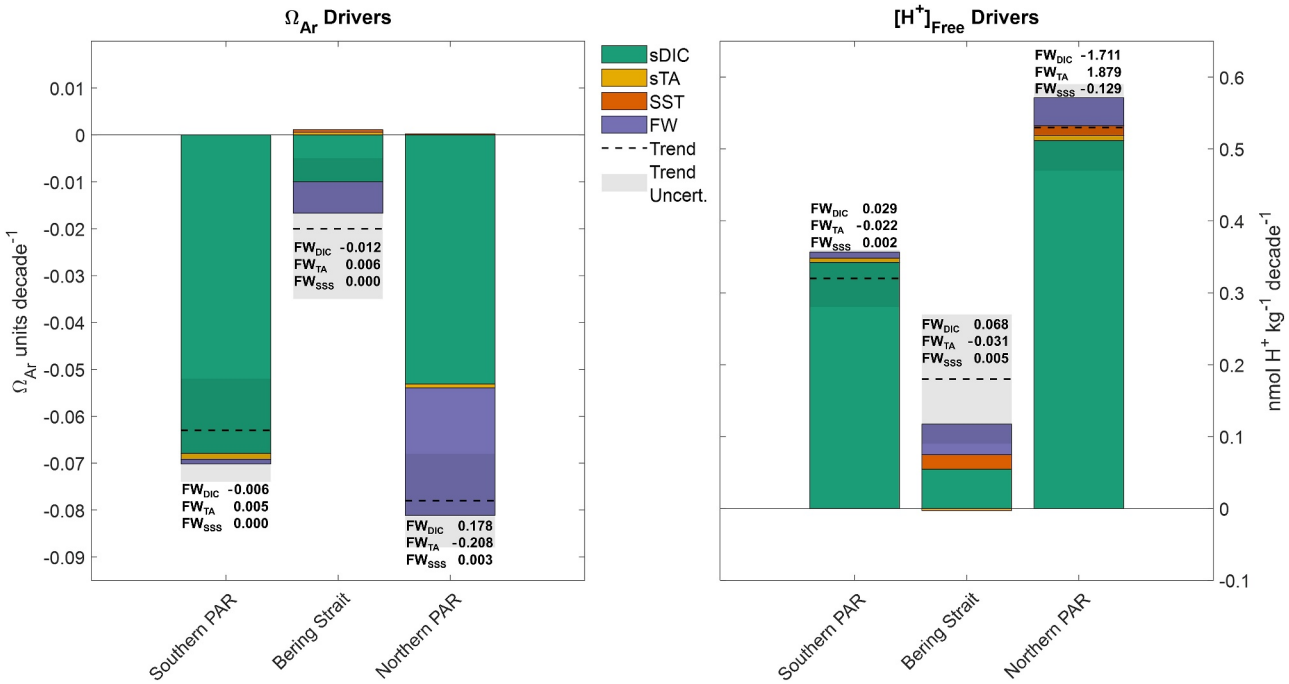

Figure 7. Area-weighted driver decomposition results for each subregion calculated using Equations 8 and 9. Only the "change in driver" terms are shown, as the change in sensitivity and mass effect terms are omitted for clarity due to their nearly equal magnitudes and opposite directions. The four drivers (sDIC, sTA, SST, and FW) are presented, with the sum of all drivers approximately equaling the total trend represented by the dashed line. For additional context, the individual components of the FW driver are also displayed.

drivers, changes in sensitivity, and mass effect and their uncertainties are provided in Table S2 in Supporting Information S1.

Southern PAR Drivers. The drivers of acidification in the Southern PAR closely matched that of the global, ice-free ocean. Effectively, the entirety of the overall Ω_{Ar} trend (-0.063 Ω_{Ar} units dec^{-1}) was accounted for by increased sDIC, which caused Ω_{Ar} to decrease by -0.068 units dec^{-1}. Changes in sTA (-0.001 Ω_{Ar} units dec^{-1}), and FW (-0.001 Ω_{Ar} units dec^{-1}) drove acidification to a negligible degree, while SST trends had an insignificant impact (0.000 Ω_{Ar} units dec^{-1}).

Similarly, the positive $[H^+]_F$ trend (0.32 nmol kg^{-1} dec^{-1}) observed in the Southern PAR was almost entirely driven by increased sDIC (0.34 nmol kg^{-1} dec^{-1}). Minuscule trends in sTA (0.01 nmol kg^{-1} dec^{-1}), SST (0.00 nmol kg^{-1} dec^{-1}), and FW (0.01 nmol kg^{-1} dec^{-1}) contributed to the increase in $[H^+]_F$, but their effect was minimal.

Bering Strait Drivers. The Ω_{Ar} decline (-0.020 units dec^{-1}) observed in the Bering Strait subregion was primarily driven by increased sDIC (-0.010 Ω_{Ar} units dec^{-1}), albeit at a much lower rate than the rest of the PAR. Similar to the Southern PAR, changes in sTA (0.001 Ω_{Ar} units dec^{-1}) and SST (0.001 Ω_{Ar} units dec^{-1}) played an insignificant role in overall Ω_{Ar} trends, though both slightly mitigated acidification. Freshwater balance played a slightly larger role and further drove acidification trends, as the net freshwater driver (FW) was -0.007 Ω_{Ar} units dec^{-1}. This is explained by the slight increase in SSS, particularly on the Bering Sea shelf (Figure 5), which increased both DIC and TA via additional dissolved ions. Although the direct effects of SSS trends on Ω_{Ar} were insignificant (FW_{SSS} = 0.000 Ω_{Ar} units dec^{-1}), the impact of freshwater balance–induced increases in DIC on Ω_{Ar} (FW_{DIC} = -0.012 Ω_{Ar} units dec^{-1}) outweighed the impact of the corresponding increase in TA (FW_{TA} = 0.006 Ω_{Ar} units dec^{-1}). This resulted in a net negative FW term that drove acidification, as the increase in SSS in the Bering Strait subregion increased DIC more than it increased TA, contributing to the decrease in Ω_{Ar}.

The $[H^+]_F$ increase (0.18 nmol kg^{-1} dec^{-1}) in the Bering Strait subregion was driven by similar factors as the Ω_{Ar} decline. Increased sDIC (0.06 nmol kg^{-1} dec^{-1}) was the main driver, closely followed by the FW term. Again, freshwater removal increased DIC (FW_{DIC} = 0.07 nmol kg^{-1} dec^{-1}) more than TA (FW_{TA} = −0.03 nmol kg^{-1} dec^{-1}) which, in conjunction with the direct effects of SSS (FW_{SSS} = 0.01 nmol kg^{-1} dec^{-1}), resulted in a net positive FW term (0.04 nmol kg^{-1} dec^{-1}) indicating that FW removal contributed to the $[H^+]_F$ increase. Minor changes in sTA slightly offset this increase (−0.01 nmol kg^{-1} dec^{-1}), while the warming trend further drove acidification (0.02 nmol kg^{-1} dec^{-1}).

Northern PAR Drivers. The Ω_{Ar} decline observed in the Northern PAR (−0.078 units dec^{-1}) was primarily driven by increased sDIC (−0.053 Ω_{Ar} units dec^{-1}). Freshwater dynamics played a more significant role in Ω_{Ar} decline in the Northern PAR than in any other subregion. Unlike the Bering Strait subregion, which experienced slight salinization, the Northern PAR exhibited strong freshening trends likely caused by sea ice melt and increased riverine discharge. On the Bering Sea shelf, DIC has a stronger relationship to SSS than TA does, meaning rising SSS caused DIC to increase more than TA. The opposite was true for the Northern PAR, where TA has a stronger relationship to SSS than DIC (Figure S3 in Supporting Information S1). As a result, a decrease in SSS caused a larger decline in TA compared to DIC. This is reflected in the FW components: FW_{TA} (−0.208 Ω_{Ar} units dec^{-1}) had a greater magnitude than FW_{DIC} (0.178 Ω_{Ar} units dec^{-1}), leading to a net freshwater-driven decline in Ω_{Ar} (FW = −0.027 Ω_{Ar} units dec^{-1}). Thus, freshening reduced TA more than DIC, further driving the observed acidification trends. Additionally, the effects of sTA (0.001 Ω_{Ar} units dec^{-1}) and SST (0.001 Ω_{Ar} units dec^{-1}) were relatively minor and did not significantly influence the observed Ω_{Ar} trends in the Northern PAR.

For observed $[H^+]_F$ trends (0.53 nmol kg^{-1} dec^{-1}) in the Northern PAR, sDIC accounted for the majority of the trend (0.51 nmol kg^{-1} dec^{-1}). Freshening contributed to acidification through decreased DIC (FW_{DIC} = −1.71 nmol kg^{-1} dec^{-1}), decreased TA (FW_{TA} = 1.88 nmol kg^{-1} dec^{-1}), and the direct effects of salinity changes (FW_{SSS} = −0.13 nmol kg^{-1} dec^{-1}), resulting in a net positive FW term (0.04 nmol kg^{-1} dec^{-1}). Although freshwater addition increased $[H^+]_F$, its impact was significantly smaller than for Ω_{Ar}. This difference arises because the sensitivities of Ω_{Ar} and $[H^+]_F$ to changes in drivers (Equations 4 and 5) can vary substantially, leading to divergent outcomes for identical changes in drivers. Trends in sTA (0.01 nmol kg^{-1} dec^{-1}) and SST (0.01 nmol kg^{-1} dec^{-1}) also contributed to the overall acidification trend, though their effects were significantly smaller than those of sDIC and FW.

5. Discussion

TA and pCO_2 Prediction Uncertainty. While our TA and pCO_2 prediction methodology performed well overall across the study region, certain locations exhibited higher error and/or bias, raising potential concerns about the validity of final trend results. However, several factors support the accuracy and robustness of our results.

Predicting chemical properties in coastal waters, particularly at high latitudes, is inherently challenging due to high natural variability and the complex interplay of physical and biogeochemical processes. Arctic coastal waters are influenced by sea ice melt and formation, seasonal river discharge, permafrost and watershed inputs, and dense biological communities. These challenges, compounded by significant data gaps, especially during winter months, contribute to prediction uncertainties.

Additionally, the contribution of weak organic acids to TA (*i.e.*, organic alkalinity) constitutes another source of TA uncertainty, particularly in estuaries and coastal waters (Hunt et al., 2024). This influence is not captured by SSS or SST data, nor is it accounted for in carbonate chemistry software such as CO2SYS. Furthermore, phytoplankton and bacterial cells have been observed to contribute as much as 19 µmol kg^{-1} to TA in our study area (Lee et al., 2021), with high spatial and likely temporal variability, further emphasizing the complexity of TA prediction in this region. Despite these difficulties, our uncertainty values align closely with those reported in the established literature, highlighting the robustness of our approach within the context of these challenges.

For example, Gregor and Gruber (2021) applied a robust cluster-regression method to predict global surface TA and pCO_2 at a 1° × 1° resolution, reporting coastal RMSE values of 45 µmol kg^{-1} for TA and 32 µatm for pCO_2, with portions of the PAR exhibiting uncertainties exceeding 35 µmol kg^{-1} and 35 µatm. Similarly, Chau et al. (2023) reconstructed global TA and pCO_2 at a 0.25° × 0.25° resolution using neural networks and

multivariate regression and achieved global coastal RMSE values of 82.0 μmol kg^{-1} for TA and 27.6 μatm for pCO_2. Additionally, the Empirical Seawater Property Estimation Routines (ESPERs) (Carter et al., 2021), another established TA prediction model, achieved a RMSE of 65 μmol kg^{-1} and an MBE of 22 μmol kg^{-1} when applied to our observational data set.

For comparison, our reported MAE values correspond to RMSE values of 40.1 μmol kg^{-1} for TA and 31.6 μatm for pCO_2, closely matching or improving upon these established methods. These comparisons demonstrate that while uncertainties remain, our results are consistent with the literature and reflect the inherent difficulty of predicting carbonate system variables in coastal and high-latitude regions. Most importantly, predictions for the PAR, despite their uncertainties, provide critical insights into an ecologically significant and data-sparse region.

Trend Uncertainty. Uncertainty and bias in TA and pCO_2 predictions are mitigated by several factors. First, bias in individual monthly predictions does not skew trend results as long as the bias is consistent. Additionally, error does not propagate linearly into calculated Ω_{Ar}, $[H^+]_F$, and pH_T values. For example, a 10% TA and 20% pCO_2 error does not necessarily result in a 30% Ω_{Ar} error, as the relationships among carbonate system variables are nonlinear. The extent to which error propagates depends on the state of the carbonate system (Equation 2), meaning the impact of a given error combination varies based on environmental conditions.

Even in areas with high error in monthly values, the bootstrapping process ensures that trend uncertainties accurately reflect these errors. While individual monthly errors (noise) can be significant, a strong underlying trend (signal) can still emerge, as the long-term trend relies on the collective behavior of all data points in the time series. This statistical averaging reduces the influence of uncertainty in any single monthly value, allowing the acidification signal to be detectable despite the noise. Trends are reported with their associated uncertainties, and if the propagated uncertainty is too large, the trend is identified as statistically insignificant. Additionally, when trends are averaged across thousands of grid cells to calculate subregion trends, the impact of outliers and localized areas of high uncertainty is minimized, providing a more robust representation of regional trends.

For example, the Beaufort Sea exhibits relatively high TA error. However, because Ω_{Ar} uncertainty is determined by the combined contributions of all input variables (TA, pCO_2, SSS, SST, Si, and PO_4^{3-}) and their respective uncertainties, the impact of TA error is diluted within the overall Ω_{Ar} uncertainty. For a single grid cell, monthly Ω_{Ar} uncertainty only moderately affects the trend uncertainty for that grid cell. When aggregating trends across the Northern PAR, the proportional contribution of grid cells from the Beaufort Sea, where TA error is higher, is small compared to the entire subregion, further reducing its influence on the overall trend uncertainty for the Northern PAR.

Uncertainty Reveals Change. The spatial distribution of TA prediction error (Figure 3a) can shed light on regions with more complex biogeochemical processes. While a strong linear correlation exists between SSS and TA, certain processes can disrupt this relationship. For instance, the formation and dissolution of calcium carbonate ($CaCO_3$) impacts TA without affecting SSS. Areas undergoing $CaCO_3$ dissolution would exhibit a rise in TA not mirrored in SSS measurements, leading to a higher prediction error. This increase in error, while highlighting a limitation in the TA prediction method's ability to accommodate salinity-independent processes, also signals underlying changes at these locations, providing valuable clues for further analysis.

Shifts in plankton species composition, particularly changes involving coccolithophores (a group of highly productive marine calcifiers) represents another salinity-independent factor that may affect TA prediction accuracy. Coccolithophores have the potential to significantly influence carbonate system dynamics. While primary productivity decreases DIC and marginally increases TA, $CaCO_3$ formation characteristic of coccolithophores reduces TA (by removing Ca^{2+}) and Ω_{Ar} (by eliminating CO_3^{2-}), as illustrated in the following reaction. This reaction also raises CO_2 levels, thereby lowering pH_T:

$$2HCO_3^-(aq) + Ca^{2+}(aq) \rightleftharpoons CO_2(g) + CaCO_3(s) + H_2O(l) \quad (12)$$

For example, the first recorded coccolithophore bloom in the Bering Strait subregion occurred during the summer of 1997 (Vance et al., 1998). Since then, such blooms have become a regular phenomenon. On the Bering Sea shelf, blooms of the coccolithophore *E. huxleyi* have been observed to decrease TA by as much as 82 μmol kg^{-1} (Murata, 2006) and 59 μmol kg^{-1} (Cross et al., 2013). Consequently, changes such as the poleward movement of

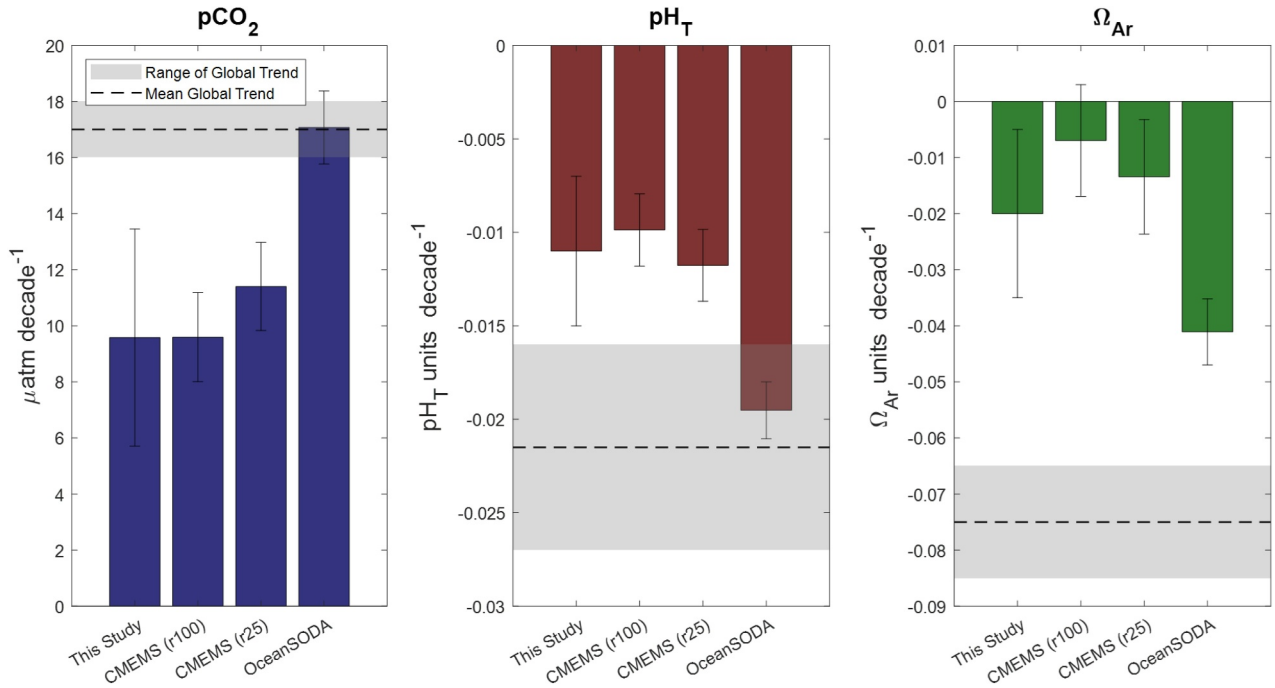

Figure 8. The bootstrapped seasonal Theil-Sen estimator was used to determine area-weighted average trends and trend uncertainties for pCO_2, pH_T, and Ω_{Ar} from 1993 to 2021 for the Bering Strait subregion. The trend methodology was applied to the CMEMSr100, CMEMSr25, and OceanSODA carbonate system data sets in order to compare the trends of this study using a consistent methodology. Error bars denote the 95% bootstrap confidence interval. The wide range in trend uncertainty arises because each data set defines monthly uncertainty differently (MAE, RMSE, ensemble mean) and should be interpreted with caution.

Atlantic-sourced coccolithophores into the Arctic (Ardyna & Arrigo, 2020) can substantially alter local carbonate system dynamics, highlighting the complex interplay between biological activity and ocean chemistry. These processes underscore how regions with high TA prediction residuals may indicate locations that warrant further investigation.

Regions exhibiting the highest TA prediction errors correspond to areas where rivers drain into the sea, such as the Beaufort Sea near the Mackenzie River discharge, the East Siberian Sea at the Kolyma River outlet, and the northern Gulf of Alaska which is influenced by the Susitna and Copper Rivers. This pattern suggests that riverine inputs significantly affect the accuracy of our TA predictions by introducing variability not accounted for by SSS and SST alone. It also supports the notion that some Arctic rivers are undergoing significant changes in chemical composition (*e.g.*, TA, nutrient concentration, dissolved organic carbon) as a result of climate change and anthropogenic activities and noted in prior work (Drake et al., 2018; Tank et al., 2023).

Southern PAR. Carbonate system trends and drivers for the Southern PAR represent the global mean state of OA. The rising sDIC driving acidification in the Southern PAR is likely attributable to anthropogenic CO_2 uptake as noted in previous work and expected in an ice-free, open-ocean environment.

Portions of the southern Alaska coast exhibited weakened or a lack of trends in pH_T or Ω_{Ar} (Figure 5). This anomaly could stem from the considerable uncertainty in pCO_2 measurements along the entire southern Alaska coast and significant TA uncertainty in the northern Gulf of Alaska, hindering the bootstrap method's ability to identify significant trends. However, coastal Alaska experiences significant runoff from land-terminating glaciers that contain higher TA than DIC (Pilcher et al., 2018). This runoff could buffer the coastal carbonate system, explaining both the weakened acidification signal and higher prediction uncertainty.

Bering Strait. Our results indicate that the Bering Strait subregion acidified significantly slower than the global mean rate, with portions of the subregion exhibiting no acidification signal at all. This challenges the prevailing literature that identifies the Bering Strait subregion as an acidification hotspot, with studies listed in Table 1 showing OA rates at or far exceeding global levels. Considering the disagreement between our Bering Strait trends and the established literature, we also applied our bootstrap trend methodology to pCO_2, pH_T, and Ω_{Ar} data

from the OceanSODA and CMEMS gridded carbonate system data sets (Figure 8). This approach enabled us to apply a consistent trend methodology to data sets that were independently produced and validated, reinforcing the robustness of our trend results even in cases where they differed from prior studies.

Cross-dataset trend results for the Bering Strait subregion show that our results are broadly consistent with the other data sets. All data sets indicated an increase in pCO_2, with our study closely matching both CMEMS data sets at 10 μatm dec^{-1}. OceanSODA also showed an increase but at a higher rate of 17 μatm dec^{-1}, consistent with the global mean. For pH_T, our data set and both CMEMS data sets indicated a decline of approximately −0.01 units dec^{-1}, while OceanSODA reported a larger decline of −0.02 units dec^{-1}, double our result and consistent with the global mean trend. This disparity in pH_T trends highlights the variability among data sets but remains within the range of plausible uncertainty. The largest differences were observed in Ω_{Ar} trends. Both CMEMS data sets showed a slower decline than our data set, while OceanSODA showed a faster decline. Despite these differences, all Ω_{Ar} trends were notably low compared to the mean global rate. This suggests that additional processes beyond carbon uptake may be mitigating Ω_{Ar} decline in the Bering Strait region. Overall, the trends for all three variables in the CMEMS and OceanSODA data sets were within or close to the uncertainty range of our results, supporting the robustness of our findings.

Our results indicate that surface pCO_2, and consequently surface DIC, increased at a significantly reduced rate despite steadily rising atmospheric CO_2 concentrations throughout the study period. This slower increase accounts for the lower-than-expected acidification rates observed in the Bering Strait subregion. Enhanced surface primary productivity, which removes inorganic carbon from surface waters and exports it to depth via the biological pump, appears to be the primary factor driving this phenomenon.

As outlined in the Study Area section, the Bering Strait subregion experiences large phytoplankton blooms due to Alaskan Coastal water and nutrient-rich Anadyr water mixing near the Bering Strait passage. This could explain why we observed a weaker acidification signal in the western and northern sectors of the Bering Strait subregion, where nutrient-rich waters drive productivity (Figure 6). Notably, the emergence of fall phytoplankton blooms, tied to delayed sea ice formation and an extended growing season, suggests that primary productivity may have also risen in tandem with decreasing sea ice extent. This hypothesis is supported by observed positive decadal trends in surface Chlorophyll *a* (Oziel et al., 2022) and annual primary production (Brown & Arrigo, 2012), as well as a biologically driven increased summer carbon sink (Wang et al., 2022b) in the Bering Strait subregion over a similar timeframe. Enhanced primary productivity may simultaneously explain the elevated acidification rates observed in Bering Strait bottom waters (Mathis et al., 2014; Pilcher et al., 2022), as organic carbon exported from the surface remineralizes at depth, increasing pCO_2 and promoting acidification.

Although our findings diverge from the established literature for this area, they highlight the complex interplay of physical and biogeochemical processes characteristic of coastal waters. Factors such as rising river alkalinity concentrations (Kaushal et al., 2013), particularly from Arctic rivers (Drake et al., 2018; Tank et al., 2023), and increasing riverine nutrient levels (V. H. Smith, 2003), may buffer coastal carbonate systems and enhance primary production, partially mitigating acidification. In some coastal regions, such as the Chesapeake Bay (Shen et al., 2020), the Gulf of Mexico (Gomez et al., 2021; Hu et al., 2015), and the coastal Netherlands (Provoost et al., 2010), these processes have even led to increases in both pH_T and Ω_{Ar}, demonstrating that elevated atmospheric CO_2 does not guarantee acidification. This underscores the need for further, ideally observational, studies on acidification in the Bering Strait subregion to better understand these trends, particularly given the region's significant economic importance as a fishery and the potential impacts of OA on marine ecosystems.

Northern PAR. Our results indicate that surface acidification rates in the Northern PAR far exceeded the global average due to a combination of anthropogenic DIC and declining TA. This contrasts with the global, ice-free ocean, where sDIC is the dominant driver of acidification, exceeding the influence of sTA, SST, or FW by an order of magnitude (Ma et al., 2023). The negative TA trend was driven by freshwater addition to the subregion, likely due to a combination of sea ice melt and increased riverine discharge, as evidenced by Figure 9 and prior studies (Qi et al., 2022; Zhang, Wei, et al., 2020). Figures 9a–9c present decadal trends (1993–2021) in sea ice thickness, SSS, and TA for the Northern PAR. The Beaufort Gyre exhibits strong negative trends in sea ice thickness (−0.8 m dec^{-1}), SSS (−1.0 psu dec^{-1}), and TA (−56.5 μmol kg^{-1} dec^{-1}), coinciding with the highest observed acidification rates in the PAR (Figure 6). Positive Pearson correlation coefficients (r) between sea ice thickness and SSS (Figure 9d) and between sea ice thickness and TA (Figure 9e) confirm the relationship among

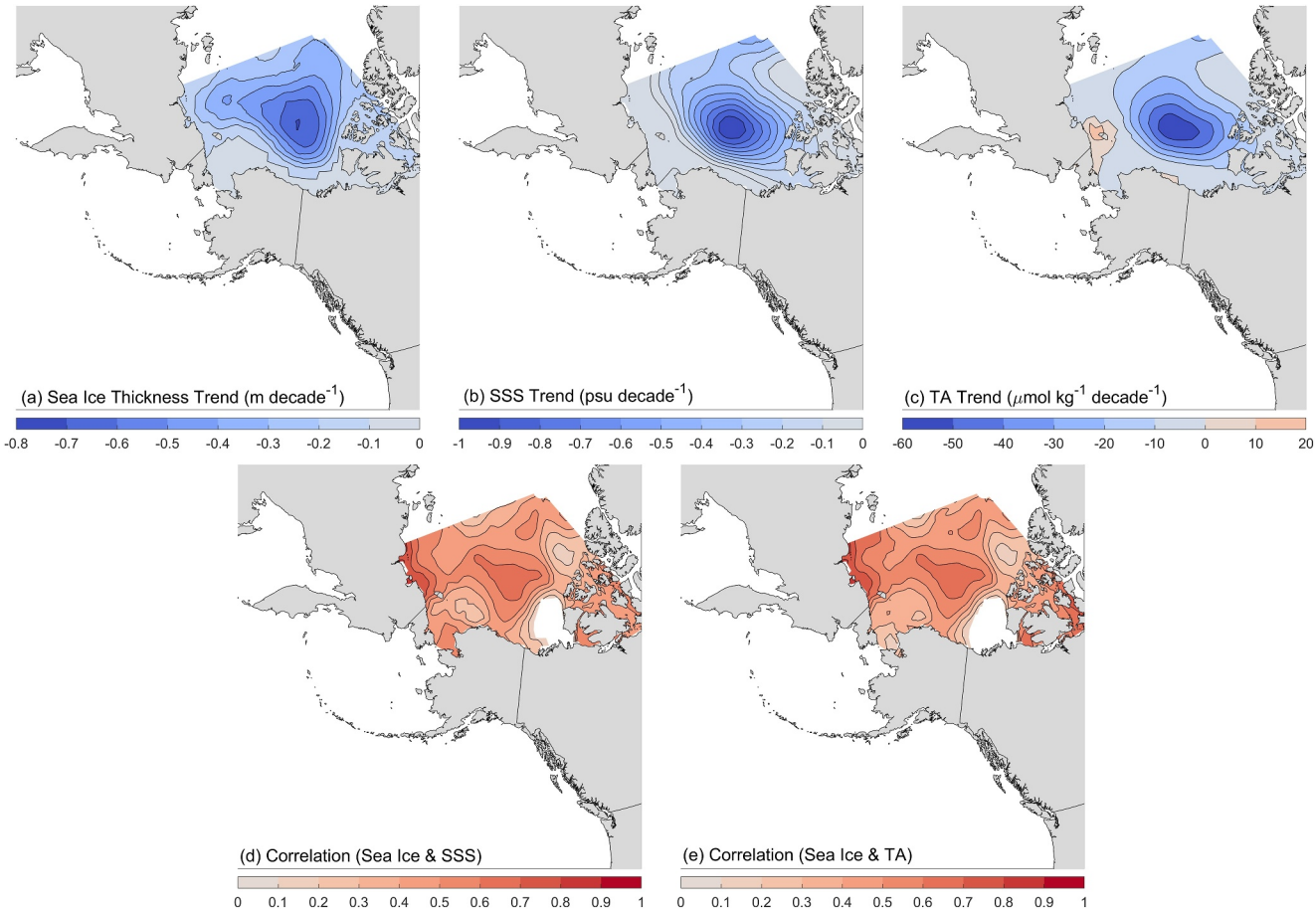

Figure 9. Decadal trends in panels (a) sea ice thickness, (b) SSS, and (c) total alkalinity (TA) for the Northern Pacific-Arctic Region from 1993 to 2021 determined using the seasonal Theil-Sen estimator. Locations with the highest rates of sea ice decline correspond to locations with strong negative SSS and TA trends. The Pearson correlation coefficient (r) between time series of ice thickness and SSS (d) and ice thickness and TA (e) statistically verify this observation. Only cells with $p < 0.05$ are plotted. The center of the Beaufort Gyre, which shows the highest rates of decline for sea ice, SSS, and TA, have r values between 0.6 and 0.7, indicating strong correlation.

these variables. The Beaufort Gyre shows r values between 0.6 and 0.7, indicating a strong correlation between ice thickness, SSS, and TA. Given that the Beaufort Gyre contains 25% of the Arctic's freshwater supply, and riverine input into the Arctic increased over the study period (IPCC, 2023; Pörtner et al., 2019), it is likely that increased riverine discharge also contributed to the freshening and subsequent acidification of the Beaufort Gyre and the Northern PAR as a whole.

Sea ice decline drives acidification through dilution and enhanced CO_2 uptake. The mechanisms by which this occurs are heavily dependent on sea ice characteristics and can be broken into three distinct phases as shown in Figure 10. Figure 10 compares time series of sea ice thickness, SSS, surface pCO_2, and air-sea carbon flux (negative being into the water) from 1993 to 2021 in the Beaufort Gyre (75°N, 215°E). Phase I (1993–1998) is characterized by year-round multi-year ice cover. Sea ice thickness declined (-1.4 m dec^{-1}), driving dilution as indicated by the negative SSS trend (-4 psu dec^{-1}). Qi et al. (2022) found that the combined effects of dilution-driven reductions in TA and DIC from sea ice melt lowers pCO_2, explaining the negative pCO_2 trend of -89 µatm dec^{-1}). Persistent ice cover prevented significant air-sea carbon flux, evidenced by near-zero flux values during Phase I. This dilution process primed surface waters underlying the ice for rapid acidification by decreasing both TA, lowering its resistance to acidification, and pCO_2, strengthening the pCO_2 gradient between underlying seawater and rising atmospheric CO_2 concentrations.

Phase II (1998–2013) marks the transition from a regime dominated by thick, multi-year ice with persistent coverage to one where thinner, seasonal first-year ice predominates, with September 1998 recording a historic low in sea ice extent that signaled the sea ice transition (Hutchings & Rigor, 2012; Zhang, Wei, et al., 2020). The

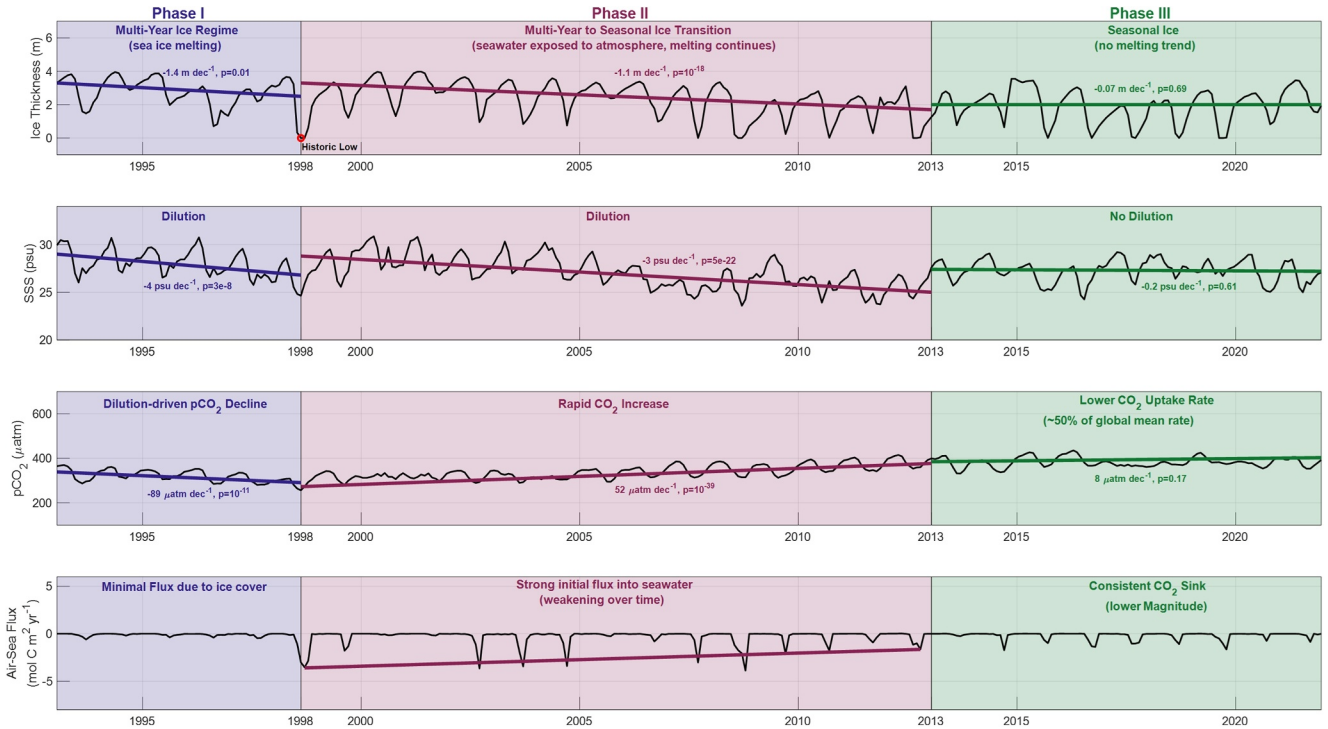

Figure 10. Time series of ice thickness, SSS, surface pCO_2, and air-sea carbon flux in the Beaufort Gyre (75°N, 215°E) from 1993 to 2021. This location corresponds to the highest observed acidification rates of the Pacific-Arctic Region. The time series is broken into three phases: Phase I is characterized by thinning ice, which lowers SSS, TA, and pCO_2 via dilution. Persistent ice cover prevents air-sea flux, enabling a negative pCO_2 trend. Phase II marks when this location is predominated by seasonal sea ice and air-sea flux can rapidly increase pCO_2 levels. Dilution stops by Phase III and the air-sea pCO_2 gradient is smaller, reducing CO_2 uptake.

remaining multi-year ice continued to melt, indicated by the ice thickness rate of -1.1 m dec^{-1}, driving further dilution as seen in the SSS trend of -3 psu dec^{-1}. Dilution-induced low pCO_2 values facilitated rapid carbon uptake due to the strong air-sea pCO_2 gradient, reversing the negative pCO_2 trend of Phase I to a positive trend of 52 µatm dec^{-1} in Phase II. This is primarily because atmospheric CO_2 could now flux into surface waters due to the exposed air-sea interface, as indicated by the large negative September spikes in air-sea flux in Phase II that were not present during Phase I. This swift uptake, alongside the dilution-driven reduction in TA during Phases I and II, primarily drove the rapid acidification observed in the Beaufort Gyre. As the air-sea pCO_2 gradient diminished, so too did the seasonal carbon flux into the sea surface and the rate of pCO_2 uptake, signaling the shift to Phase III.

Phase III (2013–2021) is characterized by a stabilization of sea ice thickness and a lack of dilution, as evidenced by p-values for ice thickness and SSS trends of 0.69 and 0.61, respectively. Surface pCO_2 levels continued to climb at a rate of 8 µatm dec^{-1}, a pace six times slower than in Phase II and about half the global average rate of 17 µatm dec^{-1}. Surface waters remained a consistent carbon sink each September, albeit at considerably reduced rates (-1.7 to -0.83 mol C m^2 yr^{-1}) compared to Phase II. Although we identified January 2013 as the boundary between Phase II and III, the actual transition likely represents a gradual, less distinct shift than the clear, stepwise shift from Phase I to II and therefore cannot be easily defined.

This phase-based framework for describing sea-ice carbonate dynamics can also explain the portion of the Northern PAR near the North Pole that exhibited a decrease in pCO_2, accompanied by an increase in pH_T and Ω_{Ar} (Figure 5). Over the period 1993–2021, this area showed statistically significant trends in sea ice thickness (-0.3 m dec^{-1}) and SSS (-0.4 psu dec^{-1}). However, sea ice thickness remained sufficiently high to avoid a transition from a multi-year to a seasonal ice regime. In other words, this area of the Northern PAR remained in Phase I, where dilution drove the observed decrease in surface pCO_2 while consistent ice cover prevented substantial CO_2 uptake.

Figure 10 does not include temperature effects on the carbonate system as they were relatively minor. Rising SST reduces the solubility of CO_2, causing some dissolved CO_2 to become gaseous, thereby increasing pCO_2. For the Beaufort Gyre, we observed no statistically significant long-term trend in SST, which is expected since the area experiences seasonal sea ice formation and remains near its freezing point (−1.8°C) for most of the year. However, when examining only September data points, we found a warming trend of 0.7°C dec^{-1} ($p = 10^{-5}$). This seasonal warming would increase summertime surface pCO_2, but its impact on long-term trends is mitigated as the water cools and ice forms again in autumn. Additionally, a higher summertime pCO_2 value would weaken the air-sea pCO_2 gradient, reducing the amount of carbon absorbed during air-sea exchange.

Our findings reveal that increased freshwater likely due to significant sea ice melt and rising riverine discharge, coupled with increasing atmospheric CO_2 levels, led to rapid surface acidification in the Northern PAR, especially in zones undergoing shifts in sea ice dynamics. This observation has two primary implications. First, the intense acidification rates observed might be a temporary condition in regions transitioning from dense, year-round ice to seasonal coverage, as depicted in Figure 10. Zhang, Yamamoto-Kawai, and Williams (2020) observed this in the Beaufort Sea, noting a decline in surface Ω_{Ar} by 0.5 units dec^{-1} from 1997 to 2007 followed by no Ω_{Ar} trend from 2007 to 2016. The second implication is that higher latitudes, currently under year-round ice cover, might undergo rapid acidification akin to Phase II of Figure 10 if their ice thins sufficiently to expose the surface waters to the atmosphere. However, the acidification rate would likely decline over time as the air-sea CO_2 gradient weakens as observed in Phase III.

6. Caveats and Limitations

Our study's primary limitation stems from the very issue it seeks to overcome: significant spatial and temporal data gaps. Figure S1 in Supporting Information S1 highlights the scarcity of carbonate system observations during the boreal spring and winter, especially in sea-ice-affected zones, with most sampling occurring in the summer and fall. This scarcity complicates, and in some locations prevents, prediction validation for spring and winter months. The complex interplay between sea ice dynamics and the carbonate system, coupled with the importance of sea ice trends to our findings, underscores the critical gap presented by the absence of field samples in these seasons. Moreover, certain areas within the PAR, such as key regions along the Russian coast and the Canadian Archipelago, suffer from a chronic lack of data throughout the year.

In addition to these observational gaps, our analysis is inherently tied to the gridded SSS and SST data sets used for TA prediction and driver decomposition. Although these SSS and SST data sets have been evaluated and validated in the literature, any error or bias inherent in them could influence our overall trend and driver results. Future efforts to conduct the same analysis with different combinations of SSS and SST data sets, or using an ensemble approach, could help address this limitation and improve the robustness of the results.

While these data gaps and potential data set biases challenge our capacity to refine and validate predictive models in some locale during certain seasons, they underscore the necessity of our efforts to reconstruct the carbonate system from the limited data that is available. Enhanced sampling efforts in the Arctic would gradually refine such predictions, sharpening our understanding of the region's evolving carbonate dynamics.

7. Conclusion

By harnessing open-source data sets across the PAR, we identified spatial relationships to predict surface TA from openly available data sets. In conjunction with the SOM-FFN surface pCO_2 data set, it was possible to resolve the full surface carbonate system on a monthly basis from 1993 to 2021. Leveraging this data set, we introduced a robust methodology for detecting and quantifying trends, marking the first effort to systematically quantify trends in surface carbonate system parameters across the PAR. This approach bridges spatial and temporal gaps in our understanding of trends outlined in Table 1. The Northern PAR lacks a publicly available comprehensive carbonate system data set, with existing resources such as CMEMS and Ocean-SODA offering limited coverage in ice-covered regions. Therefore, the surface carbonate system data set compiled in this study, as well as the discrete bottle samples, are intended to facilitate subsequent research efforts.

Our findings reveal that surface waters of the Southern PAR (an ice-free, open-ocean environment) acidified at a similar rate to the global mean, primarily due to the uptake of anthropogenic carbon. Conversely, the Bering Strait

subregion—a critical conduit for Pacific waters into the Arctic Ocean—exhibited a weakened acidification signal, likely due to enhanced primary productivity. This suggests that while the PAR in general is vulnerable to acidification, the highly productive ecosystems of the Bering and Chukchi Sea shelves acted to mitigate the effects of rising atmospheric CO_2, albeit with potential repercussions for acidification in deeper waters. Most notably, the Northern PAR experienced surface acidification rates 2–4 times higher than the global average, primarily due to anthropogenic CO_2, freshwater addition, and dynamics between sea ice and the carbonate system in zones of multi-year ice recession.

Should atmospheric CO_2 continue to rise, surface waters of the PAR will likely continue to acidify. Continued anthropogenic warming poses a significant threat to the high-latitude areas of the Northern PAR, which are currently shielded from CO_2 invasion by annually persistent sea ice. A transition in these regions from a multi-year ice cover to a dominantly seasonal, first-year ice cover could trigger rapid acidification similar to that observed in the Beaufort Gyre within this study. Although rising primary productivity, potentially driven by sea ice changes, currently seems to mitigate surface acidification in the Bering Strait subregion, it is likely that this CO_2 export from the surface will be surpassed by the influx of atmospheric CO_2, unless there is a sustained increase in primary productivity. Therefore, the weakened trends observed in the Bering Strait subregion may be temporary, with future data potentially showing faster acidification. Likewise, the Southern PAR is expected to keep acidifying as atmospheric CO_2 levels rise.

Key areas for future investigation include detailed analyses of regions with high uncertainties in pCO_2 and TA to refine trend identification. Moreover, enhancing the methodologies for predicting pCO_2 and TA, especially by explicitly incorporating seasonality, could significantly improve the accuracy of trend predictions and reduce uncertainties. Refining TA and DIC drivers into specific processes such as net community production, calcification, and anthropogenic carbon uptake (Fassbender et al., 2016; Ma et al., 2023), would offer further insight into the drivers of long-term change in the carbonate system. The results pertaining to the Bering Strait subregion, which contrast with prevailing literature, highlight a need for future work focused on understanding the mechanisms driving changes in the carbonate system of this ecologically important region.

Data Availability Statement

All data used in this work is publicly available. Discrete bottle samples for each oceanographic cruise are located at their respective DOI in Table S1. The gridded data sets used are listed, with the corresponding reference, in Table 2. The carbonate system fields created in this work (Caero et al., 2024) are available at https://doi.org/10.25921/P35D-D778.

Acknowledgments
We would like to acknowledge the vessel crews and scientists for collecting, processing, and publishing all open-source data utilized in this study. This work was conducted as part of TC's master's thesis at the University of Rhode Island Graduate School of Oceanography (URI-GSO). The URI-GSO lab startup and alumni funds afforded us the opportunity to present this work at several national and regional conferences. We greatly appreciate all members of the URI-GSO Ocean Carbon Lab for their input throughout the process, as well as Brice Loose (ORCID 0000-0002-3002-4113), Coleen Suckling (ORCID 0000-0002-8572-0909), and Carol Thornber (ORCID 0000-0003-0034-1035) for their review and feedback while serving on TC's thesis committee. Danling Ma's (ORCID 0009-0003-9291-3260) expertise in the driver decomposition process greatly aided our efforts. We also thank the SOM-FFN team for their support regarding the pCO_2 data set. AJ's contribution to the study was supported by NOAA grant NA24NESX432C0001 (Cooperative Institute for Satellite Earth System Studies—CISESS) at the University of Maryland/ESSIC. We also appreciate the thoughtful feedback and constructive comments and suggestions from two anonymous reviewers.

References

AMAP. (2013). *AMAP assessment 2013: Arctic ocean acidification*. (Tech. Rep.). Arctic Monitoring and Assessment Programme (AMAP).
AMAP. (2018). *AMAP assessment 2018: Arctic ocean acidification*. (Tech. Rep.). Arctic Monitoring and Assessment Programme (AMAP).
Ardyna, M., & Arrigo, K. R. (2020). Phytoplankton dynamics in a changing Arctic Ocean. *Nature Climate Change*, *10*(10), 892–903. https://doi.org/10.1038/s41558-020-0905-y
Bakker, D. C. E., Pfeil, B., Landa, C. S., Metzl, N., O'Brien, K. M., Olsen, A., et al. (2016). A multi-decade record of high-quality fCO2 data in version 3 of the Surface Ocean CO2 Atlas (SOCAT) [dataset]. *Earth System Science Data*, *8*(2), 383–413. https://doi.org/10.5194/essd-8-383-2016
Bates, N. R. (2006). Air-sea CO2 fluxes and the continental shelf pump of carbon in the Chukchi Sea adjacent to the Arctic Ocean. *Journal of Geophysical Research*, *111*(C10). https://doi.org/10.1029/2005jc003083
Brown, Z. W., & Arrigo, K. R. (2012). Contrasting trends in sea ice and primary production in the Bering Sea and Arctic Ocean. *ICES Journal of Marine Science*, *69*(7), 1180–1193. https://doi.org/10.1093/icesjms/fss113
Caero, T. V., Wang, H., & Jersild, A. (2024). Par-gwr-carb: A monthly gridded surface carbonate system data product for the pacific-arctic region from 1982-2021 (NCEI Accession 0292960) (Dataset No. Version 1). NOAA National Centers for Environmental Information. https://doi.org/10.25921/p35d-d778
Cai, W.-J., Chen, L., Chen, B., Gao, Z., Lee, S. H., Chen, J., et al. (2010). Decrease in the CO2 uptake capacity in an ice-free Arctic Ocean basin. *Science*, *329*(5991), 556–559. https://doi.org/10.1126/science.1189338
Caldeira, K., & Wickett, M. E. (2003). Anthropogenic carbon and ocean pH. *Nature*, *425*(6956), 365. https://doi.org/10.1038/425365a
Carstensen, J., & Duarte, C. M. (2019). Drivers of pH variability in coastal ecosystems. *Environmental Science & Technology*, *53*(8), 4020–4029. https://doi.org/10.1021/acs.est.8b03655
Carter, B. R., Bittig, H. C., Fassbender, A. J., Sharp, J. D., Takeshita, Y., Xu, Y.-Y., et al. (2021). New and updated global empirical seawater property estimation routines. *Limnology and Oceanography: Methods*, *19*(12), 785–809. https://doi.org/10.1002/lom3.10461
Chapman, W. L., & Walsh, J. E. (1993). Recent variations of sea ice and air temperature in high latitudes. *Bulletin of the American Meteorological Society*, *74*(1), 33–48. https://doi.org/10.1175/1520-0477(1993)074<0033:rvosia>2.0.co;2
Chau, T.-T.-T., Gehlen, M., Metzl, N., & Chevallier, F. (2023). CMEMS-LSCE: A global 0.25-degree, monthly reconstruction of the surface ocean carbonate system [dataset]. https://essd.copernicus.org/articles/16/121/2024/

Chen, B., Cai, W.-J., & Chen, L. (2015). The marine carbonate system of the arctic ocean: Assessment of internal consistency and sampling considerations, summer 2010. *Marine Chemistry*, *176*, 174–188. https://doi.org/10.1016/j.marchem.2015.09.007

Chen, L., & Gao, Z. (2007). Spatial variability in the partial pressures of CO2 in the northern Bering and Chukchi seas. *Deep Sea Research Part II: Topical Studies in Oceanography*, *54*(23–26), 2619–2629. https://doi.org/10.1016/j.dsr2.2007.08.010

Chierici, M., & Fransson, A. (2009). Calcium carbonate saturation in the surface water of the Arctic Ocean: Undersaturation in freshwater influenced shelves. *Biogeosciences*, *6*(11), 2421–2431. https://doi.org/10.5194/bg-6-2421-2009

Cooley, S. R., Kite-Powell, H. L., & Doney, S. C. (2009). Ocean acidification's potential to alter global marine ecosystem services. *Oceanography*, *22*(4), 172–181. https://doi.org/10.5670/oceanog.2009.106

Cross, J. N., Mathis, J. T., Bates, N. R., & Byrne, R. H. (2013). Conservative and non-conservative variations of total alkalinity on the southeastern bering sea shelf. *Marine Chemistry*, *154*, 100–112. https://doi.org/10.1016/j.marchem.2013.05.012

DeGrandpre, M., Evans, W., Timmermans, M.-L., Krishfield, R., Williams, B., & Steele, M. (2020). Changes in the Arctic Ocean carbon cycle with diminishing ice cover. *Geophysical Research Letters*, *47*(12), e2020GL088051. https://doi.org/10.1029/2020gl088051

Dickson, A. (2007). *Guide to best practices for ocean co2 measurements* (Vol. 191). PICES Special Publication.

Dickson, A., & Millero, F. (1987). A comparison of the equilibrium constants for the dissociation of carbonic acid in seawater media. Deep Sea Research Part A. *Oceanographic Research Papers*, *34*(10), 1733–1743. https://doi.org/10.1016/0198-0149(87)90021-5

Dickson, A. G. (1990). Standard potential of the reaction: AgCl(s) + 12H2(g) = Ag(s) + HCl(aq), and and the standard acidity constant of the ion HSO4- in synthetic sea water from 273.15 to 318.15 K. *The Journal of Chemical Thermodynamics*, *22*(2), 113–127. https://doi.org/10.1016/0021-9614(90)90074-Z

Doney, S. C., Fabry, V. J., Feely, R. A., & Kleypas, J. A. (2009). Ocean acidification: The other CO2 problem. *Annual Review of Marine Science*, *1*(1), 169–192. https://doi.org/10.1146/annurev.marine.010908.163834

Drake, T. W., Tank, S. E., Zhulidov, A. V., Holmes, R. M., Gurtovaya, T., & Spencer, R. G. (2018). Increasing alkalinity export from large Russian Arctic rivers. *Environmental Science & Technology*, *52*(15), 8302–8308. https://doi.org/10.1021/acs.est.8b01051

Duarte, C. M., Hendriks, I. E., Moore, T. S., Olsen, Y. S., Steckbauer, A., Ramajo, L., et al. (2013). Is ocean acidification an open-ocean syndrome? Understanding anthropogenic impacts on seawater pH. *Estuaries and Coasts*, *36*(2), 221–236. https://doi.org/10.1007/s12237-013-9594-3

Fabry, V. J., McClintock, J. B., Mathis, J. T., & Grebmeier, J. M. (2009). Ocean acidification at high latitudes: The bellwether. *Oceanography*, *22*(4), 160–171. https://doi.org/10.5670/oceanog.2009.105

Fassbender, A. J., Sabine, C. L., & Cronin, M. F. (2016). Net community production and calcification from 7 years of NOAA Station Papa mooring measurements. *Global Biogeochemical Cycles*, *30*(2), 250–267. https://doi.org/10.1002/2015gb005205

Feely, R. A., Sabine, C. L., Lee, K., Berelson, W., Kleypas, J., Fabry, V. J., & Millero, F. J. (2004). Impact of anthropogenic CO2 on the CaCO3 system in the oceans. *Science*, *305*(5682), 362–366. https://doi.org/10.1126/science.1097329

Friedland, K. D., Mouw, C. B., Asch, R. G., Ferreira, A. S. A., Henson, S., Hyde, K. J. W., et al. (2018). Phenology and time series trends of the dominant seasonal phytoplankton bloom across global scales. *Global Ecology and Biogeography*, *27*(5), 551–569. https://doi.org/10.1111/geb.12717

Friis, K., Körtzinger, A., & Wallace, D. W. R. (2003). The salinity normalization of marine inorganic carbon chemistry data. *Geophysical Research Letters*, *30*(2). https://doi.org/10.1029/2002GL015898

García, H. E., Weathers, K., Paver, C. R., Smolyar, I., Boyer, T. P., Locarnini, R. A., et al. (2019). World ocean atlas 2018, volume 4: Dissolved inorganic nutrients (phosphate, nitrate and nitrate+nitrite, silicate) [dataset]. *NOAA Atlas NESDIS*, *84*. Retrieved from https://archimer.ifremer.fr/doc/00651/76336/

Gomez, F. A., Wanninkhof, R., Barbero, L., & Lee, S.-K. (2021). Increasing river alkalinity slows ocean acidification in the northern Gulf of Mexico. *Geophysical Research Letters*, *48*(24), e2021GL096521. https://doi.org/10.1029/2021GL096521

Good, S. A., Martin, M. J., & Rayner, N. A. (2013). EN4: Quality controlled ocean temperature and salinity profiles and monthly objective analyses with uncertainty estimates [dataset]. *Journal of Geophysical Research: Oceans*, *118*(12), 6704–6716. https://doi.org/10.1002/2013JC009067

Grebmeier, J. M. (2012). Shifting patterns of life in the Pacific Arctic and Sub-Arctic seas. *Annual Review of Marine Science*, *4*(1), 63–78. https://doi.org/10.1146/annurev-marine-120710-100926

Grebmeier, J. M., Cooper, L. W., Feder, H. M., & Sirenko, B. I. (2006). Ecosystem dynamics of the Pacific-influenced Northern Bering and Chukchi Seas in the Amerasian Arctic. *Progress in Oceanography*, *71*(2), 331–361. https://doi.org/10.1016/j.pocean.2006.10.001

Gregor, L., & Gruber, N. (2021). Oceansoda-ethz: A global gridded data set of the surface ocean carbonate system for seasonal to decadal studies of ocean acidification. *Earth System Science Data*, *13*(2), 777–808. https://doi.org/10.5194/essd-13-777-2021

Gruber, N., Hauri, C., Lachkar, Z., Loher, D., Frölicher, T. L., & Plattner, G.-K. (2012). Rapid progression of ocean acidification in the California current system. *Science*, *337*(6091), 220–223. https://doi.org/10.1126/science.1216773

Hirsch, R. M., Slack, J. R., & Smith, R. A. (1982). Techniques of trend analysis for monthly water quality data. *Water Resources Research*, *18*(1), 107–121. https://doi.org/10.1029/WR018i001p00107

Honisch, B., Ridgwell, A., Schmidt, D. N., Thomas, E., Gibbs, S. J., Sluijs, A., et al. (2012). The geological record of ocean acidification. *Science*, *335*(6072), 1058–1063. https://doi.org/10.1126/science.1208277

Hu, X., Pollack, J. B., McCutcheon, M. R., Montagna, P. A., & Ouyang, Z. (2015). Long-term alkalinity decrease and acidification of estuaries in northwestern Gulf of Mexico. *Environmental Science & Technology*, *49*(6), 3401–3409. https://doi.org/10.1021/es505945p

Hunt, C. W., Salisbury, J. E., Liu, X., & Byrne, R. H. (2024). Organic alkalinity distributions, characteristics, and application to carbonate system calculations in estuarine and coastal systems. *Limnology & Oceanography*, *70*(2), 319–333. https://doi.org/10.1002/lno.12761

Hutchings, J. K., & Rigor, I. G. (2012). Role of ice dynamics in anomalous ice conditions in the Beaufort Sea during 2006 and 2007. *Journal of Geophysical Research*, *117*(C8). https://doi.org/10.1029/2011JC007182

Iida, Y., Takatani, Y., Kojima, A., & Ishii, M. (2021). Global trends of ocean CO2 sink and ocean acidification: An observation-based reconstruction of surface ocean inorganic carbon variables. *Journal of Oceanography*, *77*(2), 323–358. https://doi.org/10.1007/s10872-020-00571-5

Intergovernmental Panel on Climate Change (IPCC). (2023). Polar regions. In *Climate change 2022 – Impacts, adaptation and vulnerability: Working group II contribution to the sixth assessment report of the intergovernmental panel on climate change* (pp. 2319–2368). Cambridge University Press. https://doi.org/10.1017/9781009325844.023

Jersild, A., & Landschützer, P. (2024). A spatially explicit uncertainty analysis of the air-sea co2 flux from observations. *Geophysical Research Letters*, *51*(4), e2023GL106636. https://doi.org/10.1029/2023gl106636

Jersild, A., Landschützer, P., Gruber, N., & Bakker, D. (2017). An observation-based global monthly gridded sea surface pCO2 and air-sea CO2 flux product from 1982 onward and its monthly climatology (NCEI Accession 0160558) (Dataset No. Version 7.7). NOAA National Centers for Environmental Information. https://doi.org/10.7289/v5z899n6

Jiang, L.-Q., Carter, B. R., Feely, R. A., Lauvset, S. K., & Olsen, A. (2019). Surface ocean pH and buffer capacity: Past, present and future. *Scientific Reports*, *9*(1), 18624. https://doi.org/10.1038/s41598-019-55039-4

Kaushal, S. S., Likens, G. E., Jaworski, N. A., Pace, M. L., Sides, A. M., Seekell, D., et al. (2010). Rising stream and river temperatures in the United States. *Frontiers in Ecology and the Environment*, *8*(9), 461–466. https://doi.org/10.1890/090037

Kaushal, S. S., Likens, G. E., Utz, R. M., Pace, M. L., Grese, M., & Yepsen, M. (2013). Increased river alkalinization in the eastern US. *Environmental Science & Technology*, *47*(18), 10302–10311.

Kwok, R. (2018). Arctic sea ice thickness, volume, and multiyear ice coverage: Losses and coupled variability (1958–2018). *Environmental Research Letters*, *13*(10), 105005. https://doi.org/10.1088/1748-9326/aae3ec

Landschützer, P., Gruber, N., Bakker, D. C., Stemmler, I., & Six, K. D. (2018). Strengthening seasonal marine CO2 variations due to increasing atmospheric CO2. *Nature Climate Change*, *8*(2), 146–150. https://doi.org/10.1038/s41558-017-0057-x

Landschützer, P., Gruber, N., & Bakker, D. C. E. (2016). Decadal variations and trends of the global ocean carbon sink. *Global Biogeochemical Cycles*, *30*(10), 1396–1417. https://doi.org/10.1002/2015GB005359

Landschützer, P., Gruber, N., Bakker, D. C. E., & Schuster, U. (2014). Recent variability of the global ocean carbon sink. *Global Biogeochemical Cycles*, *28*(9), 927–949. https://doi.org/10.1002/2014GB004853

Landschützer, P., Gruber, N., Bakker, D. C. E., Schuster, U., Nakaoka, S., Payne, M. R., et al. (2013). A neural network-based estimate of the seasonal to inter-annual variability of the Atlantic Ocean carbon sink. *Biogeosciences*, *10*(11), 7793–7815. Retrieved from https://bg.copernicus.org/articles/10/7793/2013/

Lauvset, S. K., Gruber, N., Landschützer, P., Olsen, A., & Tjiputra, J. (2015). Trends and drivers in global surface ocean pH over the past 3 decades. *Biogeosciences*, *12*(5), 1285–1298. Retrieved from https://bg.copernicus.org/articles/12/1285/2015

Lauvset, S. K., Lange, N., Tanhua, T., Bittig, H. C., Olsen, A., Kozyr, A., et al. (2024). The annual update glodapv2.2023: The global interior ocean biogeochemical data product. *Earth System Science Data*, *16*(4), 2047–2072. https://doi.org/10.5194/essd-16-2047-2024

Lee, C.-H., Lee, K., Ko, Y. H., & Lee, J.-S. (2021). Contribution of marine phytoplankton and bacteria to alkalinity: An uncharacterized component. *Geophysical Research Letters*, *48*(19), e2021GL093738. https://doi.org/10.1029/2021GL093738

Lee, H., Calvin, K., Dasgupta, D., Krinner, G., Mukherji, A., Thorne, P., et al. (2023). Climate change 2023: Synthesis report. contribution of working groups i, ii and iii to the sixth assessment report of the intergovernmental panel on climate change (pp. 35–115). https://doi.org/10.59327/IPCC/AR6-9789291691647

Lehmann, C. M., Bowersox, V. C., & Larson, S. M. (2005). Spatial and temporal trends of precipitation chemistry in the United States, 1985–2002. *Environmental Pollution*, *135*(3), 347–361. https://doi.org/10.1016/j.envpol.2004.11.016

LeSage, J. P. (1999). *The theory and practice of spatial econometrics* (Vol. 28, pp. 1–39). University of Toledo.

Lewis, E. R., & Wallace, D. W. R. (1998). *Program developed for CO2 system calculations*. Environmental System Science Data Infrastructure for a Virtual Ecosystem. https://doi.org/10.15485/1464255

Ma, D., Gregor, L., & Gruber, N. (2023). Four decades of trends and drivers of global surface ocean acidification. *Global Biogeochemical Cycles*, *37*(7), e2023GB007765. https://doi.org/10.1029/2023GB007765

Mathis, J. T., Cross, J. N., Evans, W., & Doney, S. C. (2015). Ocean acidification in the surface waters of the Pacific-Arctic boundary regions. *Oceanography*, *25*(2), 122–135. https://doi.org/10.5670/oceanog.2015.36

Mathis, J. T., Cross, J. N., Monacci, N., Feely, R. A., & Stabeno, P. (2014). Evidence of prolonged aragonite undersaturations in the bottom waters of the southern Bering Sea shelf from autonomous sensors. *Deep Sea Research Part II: Topical Studies in Oceanography*, *109*, 125–133. https://doi.org/10.1016/j.dsr2.2013.07.019

Mathis, J. T., Pickart, R. S., Byrne, R. H., McNeil, C. L., Moore, G., Juranek, L. W., et al. (2012). Storm-induced upwelling of high pCO2 waters onto the continental shelf of the western Arctic Ocean and implications for carbonate mineral saturation states. *Geophysical Research Letters*, *39*(7). https://doi.org/10.1029/2012gl051574

Mehrbach, C., Culberson, C. H., Hawley, J. E., & Pytkowicx, R. M. (1973). Measurement of the apparent dissociation constants of carbonic acid in seawater at atmospheric pressure. *Limnology & Oceanography*, *18*(6), 897–907. https://doi.org/10.4319/lo.1973.18.6.0897

Mortenson, E., Steiner, N., Monahan, A. H., Hayashida, H., Sou, T., & Shao, A. (2020). Modeled impacts of sea ice exchange processes on Arctic Ocean carbon uptake and acidification (1980–2015). *Journal of Geophysical Research: Oceans*, *125*(7), e2019JC015782. https://doi.org/10.1029/2019JC015782

Murata, A. (2006). Increased surface seawater pco2 in the eastern bering sea shelf: An effect of blooms of coccolithophorid emiliania huxleyi? *Global Biogeochemical Cycles*, *20*(4). https://doi.org/10.1029/2005GB002615

Nguyen, H. M., Ouillon, S., & Vu, V. D. (2022). Sea level variation and trend analysis by comparing Mann Kendall test and innovative trend analysis in front of the Red River Delta, Vietnam (1961-2020). *Water*, *14*(11), 1709. https://doi.org/10.3390/w14111709

Orr, J. C., Epitalon, J.-M., Dickson, A. G., & Gattuso, J.-P. (2018). Routine uncertainty propagation for the marine carbon dioxide system. *Marine Chemistry*, *207*, 84–107. https://doi.org/10.1016/j.marchem.2018.10.006

Orr, J. C., Fabry, V. J., Aumont, O., Bopp, L., Doney, S. C., Feely, R. A., et al. (2005). Anthropogenic ocean acidification over the twenty-first century and its impact on calcifying organisms. *Nature*, *437*(7059), 681–686. https://doi.org/10.1038/nature04095

Ouyang, Z., Qi, D., Chen, L., Takahashi, T., Zhong, W., DeGrandpre, M. D., et al. (2020). Sea-ice loss amplifies summertime decadal CO2 increase in the western Arctic Ocean. *Nature Climate Change*, *10*(7), 678–684. https://doi.org/10.1038/s41558-020-0784-2

Ouyang, Z., Qi, D., Zhong, W., Chen, L., Gao, Z., Lin, H., et al. (2021). Summertime evolution of net community production and CO2 flux in the western Arctic Ocean. *Global Biogeochemical Cycles*, *35*(3), e2020GB006651. https://doi.org/10.1029/2020gb006651

Oziel, L., Massicotte, P., Babin, M., & Devred, E. (2022). Decadal changes in Arctic Ocean chlorophyll a: Bridging ocean color observations from the 1980s to present time. *Remote Sensing of Environment*, *275*, 113020. https://doi.org/10.1016/j.rse.2022.113020

Pilcher, D., Cross, J., Hermann, A., Kearney, K., Cheng, W., & Mathis, J. (2022). Dynamically downscaled projections of ocean acidification for the Bering Sea. *Deep Sea Research Part II: Topical Studies in Oceanography*, *198*, 105055. https://doi.org/10.1016/j.dsr2.2022.105055

Pilcher, D., Siedlecki, S., Hermann, A., Coyle, K., Mathis, J., & Evans, W. (2018). Simulated impact of glacial runoff on CO2 uptake in the Gulf of Alaska. *Geophysical Research Letters*, *45*(2), 880–890. https://doi.org/10.1002/2017gl075910

Pilcher, D. J., Naiman, D. M., Cross, J. N., Hermann, A. J., Siedlecki, S. A., Gibson, G. A., & Mathis, J. T. (2019). Modeled effect of coastal biogeochemical processes, climate variability, and ocean acidification on aragonite saturation state in the Bering Sea. *Frontiers in Marine Science*, *5*. https://doi.org/10.3389/fmars.2018.00508

Pörtner, H., Roberts, D., Masson-Delmotte, V., Zhai, P., Tignor, M., Poloczanska, E., et al. (2019). IPCC special report on the ocean and cryosphere in a changing climate. *755*. https://doi.org/10.1017/9781009157964

Provoost, P., Van Heuven, S., Soetaert, K., Laane, R., & Middelburg, J. (2010). Seasonal and long-term changes in pH in the Dutch coastal zone. *Biogeosciences*, *7*(11), 3869–3878. https://doi.org/10.5194/bg-7-3869-2010

Qi, D., Ouyang, Z., Chen, L., Wu, Y., Lei, R., Chen, B., et al. (2022). Climate change drives rapid decadal acidification in the Arctic Ocean from 1994 to 2020. *Science*, *377*(6614), 1544–1550. https://doi.org/10.1126/science.abo0383

Raimondi, L., Matthews, J. B. R., Atamanchuk, D., Azetsu-Scott, K., & Wallace, D. W. (2019). The internal consistency of the marine carbon dioxide system for high latitude shipboard and in situ monitoring. *Marine Chemistry*, *213*, 49–70. https://doi.org/10.1016/j.marchem.2019.03.001

Reynolds, R. W., Rayner, N. A., Smith, T. M., Stokes, D. C., & Wang, W. (2002). An improved in situ and satellite SST analysis for climate [dataset]. *Journal of Climate*, *15*(13), 1609–1625. https://doi.org/10.1175/1520-0442(2002)015<1609:AIISAS>2.0.CO;2

Riebesell, U., Fabry, V. J., Hansson, L., & Gattuso, J.-P. (2011). *Guide to best practices for ocean acidification research and data reporting*. Office for Official Publications of the European Communities.

Robbins, L. L., Wynn, J. G., Lisle, J. T., Yates, K. K., Knorr, P. O., Byrne, R. H., et al. (2013). Baseline monitoring of the western Arctic Ocean estimates 20% of Canadian Basin surface waters are undersaturated with respect to aragonite. *PLoS One*, *8*(9), e73796. https://doi.org/10.1371/journal.pone.0073796

Sabine, C. L., Feely, R. A., Gruber, N., Key, R. M., Lee, K., Bullister, J. L., et al. (2004). The oceanic sink for anthropogenic CO2. *Science*, *305*(5682), 367–371. https://doi.org/10.1126/science.1097403

Semiletov, I., Pipko, I., Gustafsson, Ö., Anderson, L. G., Sergienko, V., Pugach, S., et al. (2016). Acidification of East Siberian Arctic shelf waters through addition of freshwater and terrestrial carbon. *Nature Geoscience*, *9*(5), 361–365. https://doi.org/10.1038/ngeo2695

Sen, P. K. (1968). Estimates of the regression coefficient based on Kendall's tau. *Journal of the American Statistical Association*, *63*(324), 1379–1389. https://doi.org/10.2307/2285891

Shen, C., Testa, J. M., Li, M., & Cai, W.-J. (2020). Understanding anthropogenic impacts on pH and aragonite saturation state in Chesapeake Bay: Insights from a 30-year model study. *Journal of Geophysical Research: Biogeosciences*, *125*(7), e2019JG005620. https://doi.org/10.1029/2019JG005620

Smith, R. A., Hirsch, R. M., & Slack, J. R. (1982). *A study of trends in total phosphorus measurements at NASQAN stations*. US Government Printing Office.

Smith, V. H. (2003). Eutrophication of freshwater and coastal marine ecosystems a global problem. *Environmental Science and Pollution Research*, *10*(2), 126–139. https://doi.org/10.1065/espr2002.12.142

Spalding, M. D., Fox, H. E., Allen, G. R., Davidson, N., Ferdaña, Z. A., Finlayson, M., et al. (2007). Marine Ecoregions of the world: A bioregionalization of coastal and shelf areas. *BioScience*, *57*(7), 573–583. https://doi.org/10.1641/B570707

Taibi, H., & Haddad, M. (2019). Estimating trends of the Mediterranean Sea level changes from tide gauge and satellite altimetry data (1993-2015). *Journal of Oceanology and Limnology*, *37*(4), 1176–1185. https://doi.org/10.1007/s00343-019-8164-3

Takahashi, T., Olafsson, J., Goddard, J. G., Chipman, D. W., & Sutherland, S. C. (1993). Seasonal variation of CO2 and nutrients in the high-latitude surface oceans: A comparative study. *Global Biogeochemical Cycles*, *7*(4), 843–878. https://doi.org/10.1029/93GB02263

Tank, S. E., McClelland, J. W., Spencer, R. G., Shiklomanov, A. I., Suslova, A., Moatar, F., et al. (2023). Recent trends in the chemistry of major northern rivers signal widespread Arctic change. *Nature Geoscience*, *16*(9), 789–796. https://doi.org/10.1038/s41561-023-01247-7

Tassone, S., Besterman, A., Buelo, C., Walter, J., & Pace, M. (2021). Co-occurrence of aquatic heatwaves with atmospheric heatwaves, low dissolved oxygen, and low pH events in estuarine ecosystems. *Estuaries and Coasts*, *45*(3), 707–720. https://doi.org/10.1007/s12237-021-01009-x

Tassone, S. J., Besterman, A. F., Buelo, C. D., Ha, D. T., Walter, J. A., & Pace, M. L. (2023). Increasing heatwave frequency in streams and rivers of the United States. *Limnology and Oceanography Letters*, *8*(2), 295–304. https://doi.org/10.1002/lol2.10284

Timmermans, M.-L., & Toole, J. M. (2023). The Arctic Ocean's Beaufort Gyre. *Annual Review of Marine Science*, *15*(1), 223–248. https://doi.org/10.1146/annurev-marine-032122-012034

Tu, Z., Le, C., Bai, Y., Jiang, Z., Wu, Y., Ouyang, Z., et al. (2021). Increase in CO2 uptake capacity in the Arctic Chukchi Sea during summer revealed by satellite-based estimation. *Geophysical Research Letters*, *48*(15), e2021GL093844. https://doi.org/10.1029/2021gl093844

Uppström, L. R. (1974). The boron/chlorinity ratio of deep-sea water from the Pacific Ocean. *Deep Sea Research and Oceanographic Abstracts*, *21*(2), 161–162. https://doi.org/10.1016/0011-7471(74)90074-6

Vance, T., Schumacher, J., Stabeno, P., Baier, C., Wyllie-Echeverria, T., Tynan, C., et al. (1998). Aquamarine waters recorded for first time in eastern bering sea. *Eos, Transactions American Geophysical Union*, *79*(10), 121–126. https://doi.org/10.1029/98eo00083

van Heuven, S., Pierrot, D., Rae, J., Lewis, E., & Wallace, D. (2011). MATLAB program developed for CO2 system calculations. https://doi.org/10.3334/CDIAC/otg

Waga, H., & Hirawake, T. (2020). Changing occurrences of fall blooms associated with variations in phytoplankton size structure in the Pacific Arctic. *Frontiers in Marine Science*, *7*, 209. https://doi.org/10.3389/fmars.2020.00209

Walsh, J. E., & Chapman, W. L. (2001). 20th-century sea-ice variations from observational data. *Annals of Glaciology*, *33*, 444–448. https://doi.org/10.3189/172756401781818671

Wang, H., Lin, P., Pickart, R. S., & Cross, J. N. (2022a). Summer surface CO2 dynamics on the Bering Sea and Eastern Chukchi Sea shelves from 1989 to 2019. *Journal of Geophysical Research: Oceans*, *127*(1), e2021JC017424. https://doi.org/10.1029/2021JC017424

Wang, H., Lin, P., Pickart, R. S., & Cross, J. N. (2022b). Summer surface CO2 dynamics on the Bering Sea and eastern Chukchi Sea shelves from 1989 to 2019. *Journal of Geophysical Research: Oceans*, *127*(1), e2021JC017424. https://doi.org/10.1029/2021jc017424

Wiseman, W., Swenson, E. M., & Power, J. (1990). Salinity trends in Louisiana estuaries. *Estuaries*, *13*(3), 265–271. https://doi.org/10.2307/1351917

Woosley, R. J., & Millero, F. J. (2020). Freshening of the western Arctic negates anthropogenic carbon uptake potential. *Limnology & Oceanography*, *65*(8), 1834–1846. https://doi.org/10.1002/lno.11421

Wynn, J. G., Robbins, L., & Anderson, L. (2016). Processes of multibathyal aragonite undersaturation in the Arctic Ocean. *Journal of Geophysical Research: Oceans*, *121*(11), 8248–8267. https://doi.org/10.1002/2016jc011696

Xue, L., Yang, X., Li, Y., Li, L., Jiang, L.-Q., Xin, M., et al. (2020). Processes controlling sea surface pH and aragonite saturation state in a large northern temperate bay: Contrasting temperature effects. *Journal of Geophysical Research: Biogeosciences*, *125*(7), e2020JG005805. https://doi.org/10.1029/2020jg005805

Yamamoto-Kawai, M., McLaughlin, F. A., Carmack, E. C., Nishino, S., & Shimada, K. (2009). Aragonite undersaturation in the Arctic Ocean: Effects of ocean acidification and sea ice melt. *Science*, *326*(5956), 1098–1100. https://doi.org/10.1126/science.1174190

Zeebe, R. E., Ridgwell, A., & Zachos, J. C. (2016). Anthropogenic carbon release rate unprecedented during the past 66 million years. *Nature Geoscience*, *9*(4), 325–329. https://doi.org/10.1038/ngeo2681

Zhang, Y., Wei, H., Lu, Y., Luo, X., Hu, X., & Zhao, W. (2020). Dependence of Beaufort Sea low ice condition in the summer of 1998 on ice export in the prior winter. *Journal of Climate*, *33*(21), 9247–9259. https://doi.org/10.1175/jcli-d-19-0943.1

Zhang, Y., Yamamoto-Kawai, M., & Williams, W. (2020). Two decades of ocean acidification in the surface waters of the Beaufort Gyre, Arctic Ocean: Effects of sea ice melt and retreat from 1997–2016. *Geophysical Research Letters*, *47*(3), e60119. https://doi.org/10.1029/2019GL086421

Zuo, H., Balmaseda, M. A., Tietsche, S., Mogensen, K., & Mayer, M. (2019). The ECMWF operational ensemble reanalysis-analysis system for ocean and sea ice: A description of the system and assessment [dataset]. *Ocean Science*, *15*(3), 779–808. https://doi.org/10.5194/os-15-779-2019